Materials Today Bio 35 (2025) 102280

Contents lists available at ScienceDirect

Materials Today Bio

journal homepage: www.journals.elsevier.com/materials-today-bio

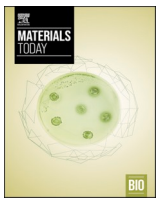

Multilayer dual-porosity 3D printed scaffolds to recreate the anisotropic microenvironment of the hyaline cartilage

Sandra Ramos-Díez [a], Luis Diaz-Gomez [b], Maria Paulis [c], Sandra Camarero-Espinosa [a,d,*]

[a] BioSmarTE Lab, POLYMAT, University of Basque Country UPV/EHU, Av. de Tolosa, 72, 20018, Donostia-San Sebastián, Spain
[b] Departamento de Farmacología, Farmacia y Tecnología Farmacéutica, I+D Farma (GI-1645), Facultad de Farmacia, Instituto de Materiales (iMATUS) and Health Research Institute of Santiago de Compostela (IDIS), Universidade de Santiago de Compostela, 15782, Santiago de Compostela, Spain
[c] Kimika Aplikatua saila, Kimika Fakultatea, POLYMAT, University of Basque Country UPV/EHU, Av. de Tolosa, 72, 20018, Donostia-San Sebastián, Spain
[d] Ikerbasque, Basque Foundation for Science, Euskadi Pl., 5, 48009, Bilbao, Spain

ARTICLE INFO

Keywords:
3D printing
Hyaline cartilage
tissue engineering
Porous scaffolds
Mesenchymal stem cells
Anisotropic structures

ABSTRACT

Articular cartilage accounts for a multizonal structure with distinct matrix composition and chondrogenic phenotypes, responsible for the tissue's load-bearing ability. Upon damage, cartilage is clinically treated by microfracture, which allows bone marrow exudation to the previously abraded zone. However, mesenchymal stem cells (hMSC) of the marrow cannot differentiate into specific chondrogenic phenotypes and the resulting tissue is isotropic and non-functional. Here, we developed multilayer dual-porosity scaffolds with defined in-fiber and structural porosities that were able to steer hMSC's differentiation into specific chondrogenic phenotypes. A library of inks prepared from poly-(*L*)lactide-co-caprolactone and sacrificial gelatine microspheres of three different diameters (13 ± 8 μm, 24 ± 14 μm, and 47 ± 27 μm) were used to 3D print structures with different patterns (90°, 60° and 45°), giving rise to dual-porosity structures of tunable in-fiber and structural porosities. This pallet of structures allowed control over porosity, topography and mechanical properties (ranging from 3.1 ± 0.1 to 9.1 ± 1.8 kPa), which modulated cell adhesion, proliferation and differentiation. Multilayer scaffolds were fabricated from selected structures that promoted chondrogenic differentiation with distinct expression of collagen type I, type II (up to 9.9 fold-increase), aggrecan and versican genes, resulting on a tissue with characteristic collagen I and II deposition patterns, abundant glycosaminoglycan deposition (15.4 ± 2.0 $\mu g_{GAG} \cdot \mu g^{-1}_{DNA}$) and similar compression modulus to native cartilage (501.5 ± 72.7 kPa).

1. Introduction

Articular cartilage is the connective tissue that covers the epiphysis of long bones, such as the femur, tibia or humerus, bearing the high loads applied during motion and protecting the bones from wear and tear. The load-bearing ability of hyaline cartilage is a consequence of the anisotropic organization of the main extracellular matrix (ECM) components (e.g., collagens and glycosaminoglycans (GAG)) through the tissue, creating what is considered a multizonal structure [1]. The zonal organization of cartilage has associated heterotypic chondrocytes, responsible of the deposition and homeostasis of these distinct areas [2–5]. Upon damage, hyaline cartilage is not capable of self-regenerating into a tissue with the characteristic anisotropic structure and thus, the mechanical properties become unpaired, leading to further damage and progression of the defect [6,7].

Current clinical treatments have been mainly focused on the implantation of autologous cells (autologous chondrocyte implantation and matrix-induce chondrocyte implantation; ACI, MACI) or on microfracture techniques [8]. These methods have in common the aim of recellularizing the damaged tissue with phenotypically coherent cells. However, the infiltrated cells are exposed to a non-regulated inflammatory microenvironment that prevents proper cell organization and phenotypic specification. Thus, the newly formed tissue lacks the coherent multizonal structure present on the native one, being unable to withstand the applied loads. This, results on long-term failure of the regenerated tissue, requiring several surgical interventions over time [9].

Tissue regeneration is based on the fabrication of scaffold materials

* Corresponding author. BioSmarTE Lab, POLYMAT, University of Basque Country UPV/EHU, Av. de Tolosa, 72, 20018, Donostia-San Sebastián, Spain.
E-mail addresses: sandra.ramos@ehu.eus (S. Ramos-Díez), luis.diaz.gomez@usc.es (L. Diaz-Gomez), maria.paulis@ehu.es (M. Paulis), sandra.camarero@ehu.eus (S. Camarero-Espinosa).

https://doi.org/10.1016/j.mtbio.2025.102280
Received 3 July 2025; Received in revised form 20 August 2025; Accepted 2 September 2025
Available online 3 September 2025

that can recapitulate some of all aspects of the targeted organ, including structure, chemistry or topography and, thus, it appears as an ideal alternative to tackle the issues associated to surgical treatments of chondral defects. Amongst the different strategies studied, the fabrication of 3D printed scaffolds that could be implanted and populated by endogenous stem cells presents several advantages. Especially noteworthy are the ease of fabrication and the tunability of parameters, the employed material, the targeted mechanical properties and the size and shape of the produced implant. 3D printed scaffolds can be fabricated at patient's size and shape and can be implanted by press-fitting without the need of further modifications [10,11]. Latest research has been mainly focused on the creation of multilayer 3D printed scaffolds that mimic different aspects of the anisotropy of the tissue. Various studies have demonstrated the capacity of varying the printing patterns (pore shape and size) to tune cell differentiation while allowing to modulate the mechanical properties of the overall 3D printed structure [12–15]. Others have investigated the potential of mimicking the biochemical properties spatially [16]. Specifically, they included gradients of kartogenin and methacrylation degree of hydrogels [17], superparamagnetic hydroxyapatite nanorods [18], chondrogenic factors with defined degradation rates [19], or clickable peptide gradients to guide the differentiation of hMSC [20]. While these studies highlight the importance of creating multilayer scaffolds that mimic the microenvironment of the targeted tissue, using biochemical gradients might suppose a challenge for clinical translation. In fact, the complicated functionalization routes of the materials and the biological impact that these molecules might have on the surrounding tissues after degradation have to be consider. Thus, other strategies to modulate cell phenotype and tissue formation with lower barriers for translation would be beneficial.

It is well-established that topography can alter cell phenotype in a relatively controlled manner, however most of the studies have so far been conducted on 2D substrates due to the difficulties of introducing topography onto 3D systems [21–24]. Some studies have tackled this challenge by introducing porosities in 3D printed scaffolds via thermally induced phase separations that effectively modulate the topography of the scaffold fibers [25,26]. However, this route difficults the incorporation of topography or porosity gradients that can drive a cartilage layer-specific cell differentiation.

Here, we hypothesized that fabricating multilayer dual-porosity scaffolds with in-fiber and structural pores, would enable the control of topography, mechanical properties and, hence, the differentiation of hMSC towards specific chondrogenic phenotypes. Specifically, we exploited a strategy based on sacrificial templates that allowed us to control all these structural parameters. After screening for different in-fiber and structural pores, we selected those that enabled the differentiation of hMSCs to specific chondrogenic phenotypes and created multilayer scaffolds with a layer dependent cell phenotype and matrix deposition.

2. Results and discussion

2.1. Scaffold design and fabrication

The pore size and shape of 3D printed scaffolds is known to play a key role in the differentiation of seeded (stem) cells [12,14,27]. Several studies have also demonstrated the capacity of porous scaffolds prepared by particle leaching, phase separation and freeze-drying, amongst others, to modulate cell proliferation, morphology and differentiation [25,28]. Here, we designed 3D printed scaffolds with dual-porosity, structural and on-fiber, to better tune the proliferation and differentiation of seeded stem cells towards the regeneration of the osteochondral interface. As a matrix, a poly-(*L*)-lactide-co-caprolactone (PLCL) polymer was chosen for its elasticity, resilience and biodegradability properties., which have been highly reported in the literature [26,29–32]. A 95 % weight loss was recorded after 45 h of incubation in a model media for accelerated degradation (Fig. S1, Supplementary Information). The PLCL used here accounts for a 70/38 (*L*)-lactide:ε-caprolactone ratio, resulting in a semicrystalline polymer [26]. The polymer's high (*L*)-lactide content enhances its rigidity. Poly (L)-lactide is a polymer prone to high degrees of crystallization, and thus, the inclusion of (L)-lactide monomer in PLCL increases the crystallinity. An increase in the degree of crystallization results in an increased rigidity and delayed biodegradation time, as compared to polycaprolactone homopolymer. Thus, the dual-porosity scaffolds described here, are expected to have an onset of degradation that occurs later than the formation of cartilage (6–12 weeks) and during the remodelling phase of the clot formed during implantation using microfracture [2].

Several studies have used solvent casting and particle leaching or phase segregation methods to fabricate porous scaffolds for tissue engineering that have the capacity to modulate cell proliferation, morphology and differentiation [28,33–35]. The pore size of these scaffolds is determined by the diameter of the employed porogen, allowing to tune the pore size among a wide range of sizes from nanometers to micrometres. The pore size plays an important role in the mechanical properties of the tissue engineered (TE) construct, which in turn, modulates the cell response in terms of phenotype, protein deposition or gene expression and epigenetics [36,37]. Here, we synthesized gelatine microspheres (GMS) with three different diameters, acting as spherical porogens in the 3D printed scaffolds. The gelatine was selected as the porogen material due to its gelation point, low cost and ease of lixiviation.

GMS were prepared by a water-in-oil emulsion process that enabled tuning the size of the particles in function of the initial concentration of gelatin and the water-to-oil ratio. GMS were fabricated starting from gelatin solutions of 10 %, 20 %, or 30 % (w/v) concentration in distilled water, yielding particles of 13 $\pm$ 8 μm, 24 $\pm$ 14 μm, and 47 $\pm$ 27 μm diameter, respectively (Fig. 1A). Although the particle diameter is slightly dispersed when using this specific water-in-oil emulsion process, the diameter of the different groups was statistically different and highly reproducible across batches (Fig. S2 and S3, Supplementary Information). As expected, an increasing particle diameter was measured with increasing gelatin concentration as a result of the higher viscosity of the solution that was stabilized with an equal concentration of surfactant. The relationship between the viscosity of the oil-in-water emulsion components and the particle diameter in GMS was previously evaluated by Nakas et al., who reported the same trend. They demonstrated that the variation in gelatine concentration, the surfactant type, the viscosity of the oil phase or the emulsification speed and time resulted in the fabrication of GMS of varying diameters between 150 and 400 μm [38]. Negrini et al. reported a GMS particle diameter closer to the ones prepared here, with an average diameter of 70.9 μm in the dry state [39]. Here, we fabricated GMS with smaller, larger, and similar diameters to the average size of 24 μm reported for MSC [40], which will allow the investigation of the role that this pore diameter range plays in cartilage regeneration.

Inks for 3D printing were prepared by mixing the GMS of different diameters (namely 13, 24 and 47 μm) at different concentrations (20 %, 30 %, 40 %, and 50 % (w/v)) on a solution of PLCL in a highly volatile solvent. To evaluate the printability of the composite inks, we measured their viscosity and storage and loss moduli, revealing an increase in these parameters with inks containing larger microspheres and higher concentrations of GMS (Fig. 1B). Some examples of this behaviour were reported in the literature, where the rheological properties of slurry materials increased with higher particle volume fractions due to superior friction between the microspheres. Furthermore, for all compositions the inks exhibited a higher storage than loss modulus, indicating an "elastic solid" behaviour. These materials have the capacity to store energy elastically and deform themselves reversibly under load [41]. Moreover, it was shown that microspheres with different sizes did not have significant viscosity differences at lower volume fractions of particles, having similar microsphere friction and rheological properties

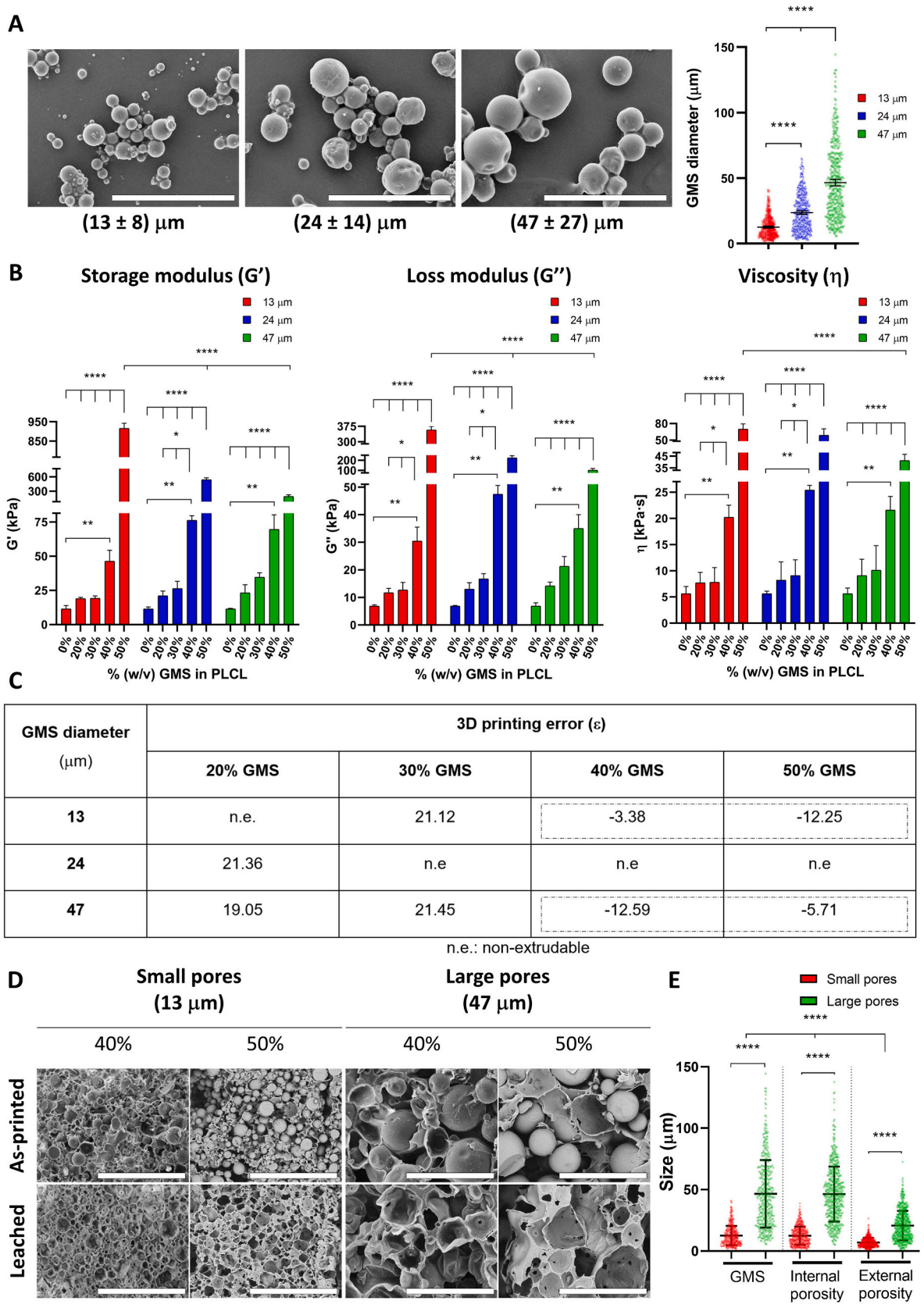

C

GMS diameter (μm)	3D printing error (ε)			
	20% GMS	30% GMS	40% GMS	50% GMS
13	n.e.	21.12	-3.38	-12.25
24	21.36	n.e	n.e	n.e
47	19.05	21.45	-12.59	-5.71

n.e.: non-extrudable

(caption on next page)

Fig. 1. Structural properties of GMS, composite inks and 3D printed scaffolds. (A) *(left)* Scanning Electron Microscopy (SEM) images of GMS produced from 10 %, 20 %, and 30 % gelatine solutions, with the average diameter ± 95 % CI. Scale bar is 200 μm in all the images. (*right*) Descriptive statistics of GMS particle diameter (μm) in triplicate batches taken from the SEM images of the small (red), medium (blue) and large GMS (green). Error bars show average ± standard deviation. (B) Rheological measurements of the composite inks as a function of the porogen size (13 μm in red, 24 μm in blue, and 47 μm in green) and GMS concentration (w/v) from 0 to 50 %. Storage (G', left) and loss (G'', middle) moduli at 4.0 Hz frequency, and viscosity (η, right) at 0.2 s^{-1} shear rate. Error bars show average ± standard deviation. Statistical significances of rheological properties (n = 3) measurements were calculated from one-way ANOVA with *posthoc* Tukey's multiple comparison tests; (****) $p < 0.0001$, (***) $p < 0.001$, (**) $p < 0.01$, and (*) $p < 0.1$ was used. (C) 3D printing error (ε) for composite scaffolds in function of the porogen loading percentage and particle diameter. Dotted-line boxes show composite inks with lower printing errors. n.e = Non-extrudable ink. (D) SEM images of scaffolds cross-sections fabricated with different GMS diameters and loading before (as-printed) and after leaching (leached), showing the GMS diameter and shape within the polymeric structure, and the formed pore. Scale bar is 200 μm. (E) GMS diameter (taken from Fig. 1A) and the internal and external pore diameter in leached scaffolds measured from SEM images. Error bars show average ± standard deviation. Statistical significances of GMS diameter (n = 350) and pore diameter (n = 600) measurements were calculated from one-way ANOVA with *posthoc* Tukey's multiple comparison tests; (****) $p < 0.0001$, (***) $p < 0.001$, (**) $p < 0.01$, and (*) $p < 0.1$ was used. (For interpretation of the references to color in this figure legend, the reader is referred to the Web version of this article.)

[42]. However, a variation in this trend was observed for our inks when a 40 % GMS loading threshold was exceeded. This behaviour was previously reported in wet granular materials containing a high percentage of solid particles. Thus, composite inks with smaller particles have higher rheological properties due to their larger surface area and, hence, resistance to flow [43].

Furthermore, the composite inks presented shear-thinning behaviour, an essential requirement for extrusion-based 3D printing (Fig. S4, Supplementary Information). Inks with shear-thinning behaviour present lower viscosity when a shear stress is applied, and increases when the shear stress is removed [44,45]. Despite observing a shear-thinning behaviour in all ink compositions under the parallel plate configuration of the rheometer, those based on middle-sized GMS diameters (24 μm) were non-extrudable at particle loading concentrations above 20 % (Fig. S5, Supplementary Information). As has been shown previously for granular hydrogels, particle jamming can substantially change the viscoelastic properties of the inks, rendering them non-extrudable under certain printing conditions. Particle packing is dependent on particle concentration and diameter and affects printing parameters such as the required printing pressure or minimum nozzle diameter. Thus, inks prepared with the same materials and equal particle loading, will behave differently if the particle diameter varies [46]. Similarly, inks composed of small GMS (13 μm diameter) at a lower loading concentration of 20 % resulted also in non-extrudable inks. In those cases, there was a substantial packing of the GMS in the printer tip that hindered their extrusion into continuous fibers. Hence, these ink compositions were discarded for the next experiments.

3D printing of composite inks gave as result scaffolds with different 3D printing errors (Fig. 1C) as revealed by morphological studies of the top and cross-sectional view (Fig. S5A, Supplementary Information). The lowest printing errors were achieved during the extrusion of inks with loaded the smallest (13 μm diameter) and the largest particles (47 μm diameter) at 40 % and 50 % GMS loading in PLCL. As aforementioned, these composite inks have the behaviour of wet granular materials. Thus, inks with higher microsphere loading account for higher viscosity due to particle friction and, in consequence, better shape retention and self-standing capacity [47]. Moreover, the lower percentage of solvent in the ink (lower percentage of polymer solution) results on a faster drying of the scaffolds, favoring shape retention (Fig. 1C and Fig. S5A, Supplementary Information). Contrarily, the scaffolds with a lower percentage of GMS in their composition (20 % and 30 % loading) did not exhibit a defined fiber structure.

Dual-porosity scaffolds were then manufactured by removal of the sacrificial GMS via lixiviation, allowing the formation of an interconnected pore structure of defined sizes within the scaffold fibers. Morphological evaluation of the printed scaffolds was performed before and after the lixiviation of GMS to assess the integrity of the particles after the printing process and the porosity generated after their removal (Fig. 1D). The shape, size and homogeneous distribution of the GMS were maintained after the ink extrusion, with no significant difference between the diameter of the particles before and after extrusion (Fig. 1E). Removal of GMS was achieved by lixiviation in water at 40 °C, which was tracked over time by measuring the nitrogen content (present only on the gelatin phase) via elemental analysis (Table S1, Supplementary Information). This correlated with morphological analysis of the lixiviated scaffolds that presented an internal porosity that matched well with the diameter of the sacrificed GMS (Fig. 1D and E). However, the diameter of the pores presented on the surface of the lixiviated scaffolds was significantly smaller than the pore diameter on the cross-section of the scaffold fiber and than the pristine GMS. This is expected as the GMS present at the scaffold surface are partially surrounded by the PLCL solution and not fully embedded.

2.2. Surface roughness on dual-porosity scaffolds modulates hMSC adhesion and proliferation

The inclusion of porosity in tissue engineering scaffolds appears as an important requirement to enhance the cell attachment. In particular, small pores with diameters lower than 100 μm have demonstrated their capacity to modulate cell adhesion *in vitro*, promoting also an early tissue formation in the cultured scaffolds [48]. Moreover, hMSC are able to migrate through pores of 12 μm or bigger [49]. Thus, a pore size ranging from 12 to 100 μm could enhance cell attachment and migration in the scaffolds. Furthermore, it has been demonstrated that the confinement of hMSC in small pores, mimicking the chondrocytes' natural environment, i.e. the chondron (accounting for diameters between 14 and 64 μm), can regulate their phenotype through cytoskeletal reorganization [50]. Hence, control of the pore diameter and scaffold porosity can determine the fate of the hMSC as it occurs in the different zones of the cartilage. On cartilage, the highest chondrocyte proliferation is observed in the superficial cartilage (persistent phenotype), followed by the middle zone (proliferative chondrocytes), and further by the deep layer (hypertrophic behavior) [2].

To evaluate the influence that our different pore sizes had on cell adhesion and proliferation, hMSC were cultured for short- (3 days) and long-term (21 days) on 3D printed dual-porosity scaffolds under basal conditions. Non-porous PLCL scaffolds were fabricated by traditional fused deposition modelling (from the melt), without sacrificial GMS template, and used as control (Fig. S6, Supplementary Information). Cells cultured on dual-porosity scaffolds with large pores (47 μm) exhibited higher hMSC adhesion than the scaffolds with smaller pores (13 μm) and non-porous scaffolds after 3 days of culture, referring to the projected area of the cells (Fig. 2A). The attachment of cells to different substrates is directed through the specific interactions of integrin pairs or through other cell surface receptors with proteins adhered to the substrate and further modulated by the chemistry, topography and mechanical properties [51–55]. The chemistry of the material of the manufactured scaffolds was the same for all the compositions, but the surface pore size and roughness was higher in the case of the scaffolds with large pores (Fig. 1E and Fig. S5B, Supplementary Information). After 3 days of culture, cells adhered to non-porous and dual-porosity scaffolds with small and large pores, with a cell surface spread area that appeared to be higher on cells cultured on large pores_50 % scaffolds. After 21 days of culture, it was observed that scaffolds with larger

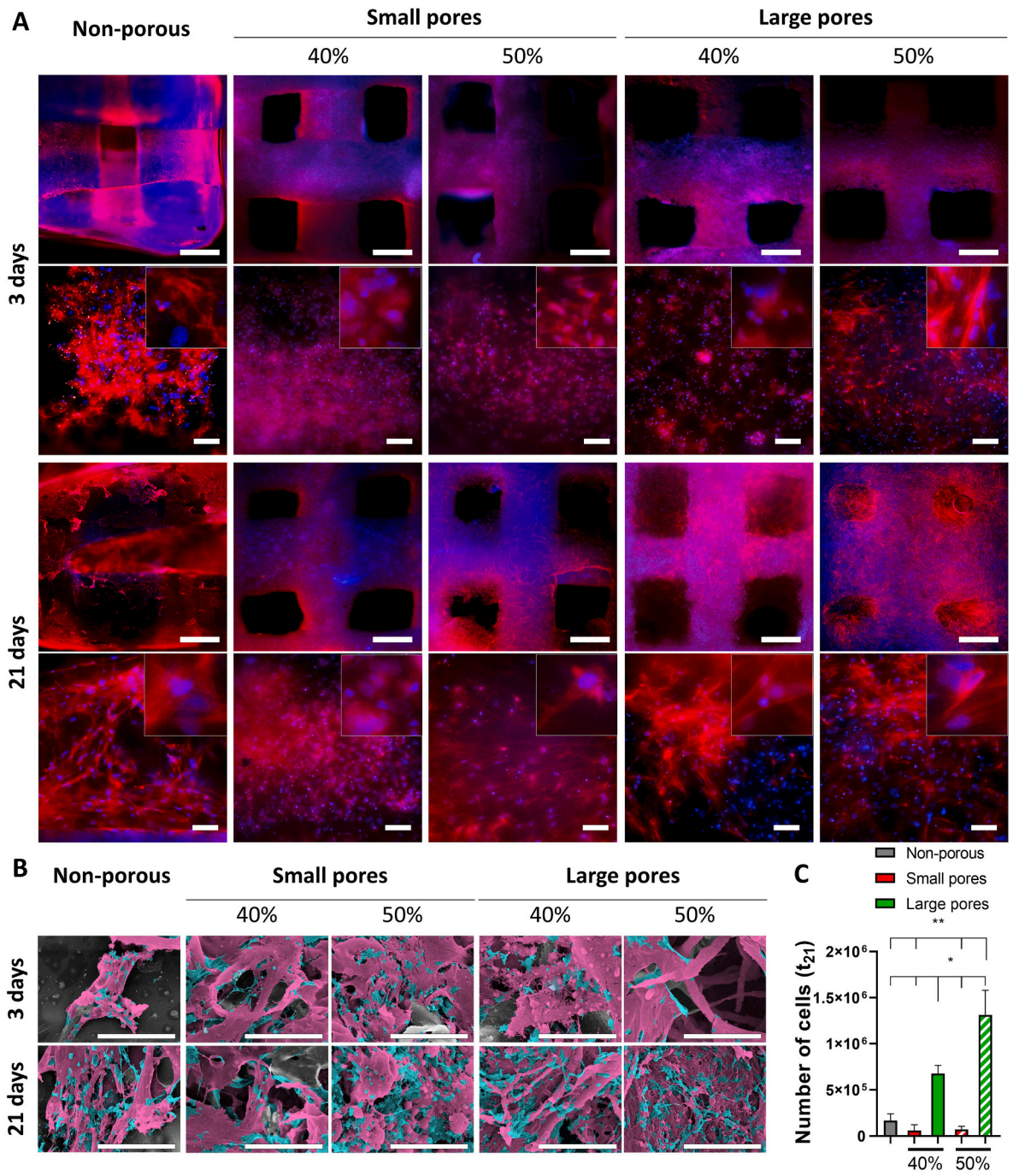

Fig. 2. Cell adhesion and proliferation capability in dual-porosity 3D printed scaffolds. (A) Fluorescence microscopy images of hMSC cultured for 3 and 21 days on non-porous constructs and dual-porosity scaffolds with different particle diameter and GMS loading stained for Hoechst-33342 (blue, nuclei) and Phalloidin-633 (red, F-actin fibers). Scale bar is 1 mm in the lower magnification images (first and third rows), and 100 μm in the higher magnification images (second and fourth rows). Inset size is 75 × 75 μm. (B) SEM images of hMSC seeded scaffolds after 3 and 21 days of culture showing cell morphology (colored in pink) and ECM deposition (colored in blue). Scale bar is 30 μm. (C) Number of cells calculated from the DNA assays after 21 days of hMSC culture in non-porous and dual-porosity scaffolds. Error bars represent standard deviation. Statistical significance (n = 3) was calculated from a one-way ANOVA with *posthoc* Tukey's multiple comparison tests; (****) $p < 0.0001$, (***) $p < 0.001$, (**) $p < 0.01$, and (*) $p < 0.1$ was used. (For interpretation of the references to color in this figure legend, the reader is referred to the Web version of this article.)

pores, both 40 % and 50 % composition, had an increased cell spread area compared with the small pores scaffolds (Fig. 2A, B and Fig. S8, Supplementary Information).

Together with the different cell spread areas observed, a difference in the amount of cells attached to the scaffolds was also apparent after 3 and 21 days of culture (Fig. 2C and Fig. S7), as quantified from the total DNA content and the number of nuclei present on the scaffold fibers. Moreover, after 21 days of culture, hMSC invaded the structural pores of the scaffolds on samples with higher pore diameter and loading (large pores_50 %), indicating an increased proliferation of the attached cells (Fig. S9 and S10, Supplementary Information). This observation was verified by quantifying the cell number (Fig. 2C). After 3 weeks of culture, the number of cells on scaffolds with smaller pores at 40 % and 50 % particle loading was not significantly different, with $6.0{\cdot}10^4$ ±

$0.4{\cdot}10^4$ cells and $7.0{\cdot}10^4 \pm 0.2{\cdot}10^4$ cells, respectively. Similarly, the non-porous scaffolds exhibited a number of cells of $1.6{\cdot}10^5 \pm 0.8{\cdot}10^5$. However, the scaffolds with large pores contained $6.8{\cdot}10^5 \pm 0.6{\cdot}10^5$ cells and $1.3{\cdot}10^6 \pm 0.2{\cdot}10^6$ cells for the 40 % and 50 % loading, respectively, an order of magnitude difference. The scaffolds with large pores and 40 % GMS loading present a lower area/volume ratio (pore surface density) compared to scaffolds of the same pore size and a higher GMS loading of 50 % (Fig. S11B, Supplementary Information). This lower surface area/volume ratio could be responsible for the lower proliferation of the hMSC in the TE constructs. Furthermore, the higher cell spread area observed in the scaffolds with larger pores could have promoted the higher proliferation observed in these scaffold compositions.

2.3. *Patterning the structure of dual-porosity 3D printed scaffolds enables tuning the mechanical properties*

The mechanical properties of the 3D printed scaffolds depend on the material they are fabricated with, the printing pattern or macrostructure given during the manufacturing process (fiber diameter, pore size and shape and layer thickness) and, if existent, the fiber's internal structure (porosity and pore size and shape) [26,56,57]. Thus, the mechanical properties of dual-porosity scaffolds fabricated from the same material and the same fiber internal structure can be modified using different 3D printing patterns. This can be exploited to mimic the native compressive properties of the different cartilage zones. The hypertrophic layer of the cartilage exerts more resistance to compression, having a higher Young's modulus than the rest of the zones (2.10 ± 2.69 MPa). Contrarily, the persistent (or superficial) zone is the softest layer (0.079 ± 0.039 MPa) and the proliferative zone presents intermediate compressive properties (1.14 ± 0.44 MPa) [58–60]. Moreover, pore shape on 3D printed scaffolds has also been suggested to affect the speed at which the pores are covered with cells, the kinetics of tissue deposition and the cell cytoskeletal organization [61–63], which altogether affect cell differentiation [12–14,25]. Printing patterns of 90°, 60° and 30° have already been reported on the literature and evaluated for their chondrogenic potential, showing a decrease in the deposition of characteristic chondrogenic proteins (GAGs and collagens) with decreasing printing pattern angle [14]. Thus, we investigated dual-porosity scaffolds using different 3D printing patterns (with deposition angles of 90°, 60° and 45°) and fiber internal porosities (small or large pores at 40 % and 50 % GMS loading) to mimic better the differences observed in the native tissue when combined into a multilayer scaffold.

Morphological evaluation of 3D printed scaffolds by SEM revealed that scaffolds with a 90° printing pattern had larger structural pores, defined as the space between deposited fibers (Fig. 3A). The deposition of a homogeneous structure with through-depth aligned porosity resulting from 90° printing patterns and, hence, lower tortuosity, resulted in a faster evacuation of the solvent and, consequently, a better shape fidelity. Similarly, scaffolds with higher tortuosity presented the smallest structural pore sizes, as a consequence of a slower solvent evaporation. As explained earlier, the fiber's internal porosity affected the shape fidelity, with an increasing shape fidelity in the scaffolds with higher GMS loading (small pores_50 % and large pores_50 %). As expected, the inks with higher ratios of GMS had the highest viscosities, showing a correlation between these parameters.

After removal of the GMS, we evaluated the compressive modulus of the scaffolds (Fig. 3B). The compressive moduli decreased for scaffolds with lower fiber internal pore size and higher particle loading. Smaller particles organize into packed structures with a smaller void space (higher packing density) than larger particles. Here, the void space is filled with polymer becoming the structure of the scaffold. Hence, the use of GMS with larger particle diameters leads, after lixiviation, to a polymer structure of thicker walls that is more resistant to compression. In particular, small pore scaffolds had compressive moduli in the 0.3–0.9 kPa range (except small pore_40 % with the 90° printing pattern whose modulus was 8.5 ± 1.4 kPa), while large pore constructs showed compressive moduli in 1.4–14.7 kPa range. As expected, the higher the percentage of porosity within the scaffold fibers (higher GMS loading), the lower the mechanical properties due to the decreased polymer content. This trend was generally observed in all dual-porosity scaffolds, except between the small pore scaffolds with a 45° printing pattern, where no significant differences were detected between 40 % and 50 % GMS loading. Finally, evaluating the mechanical differences between scaffolds with the same composition but different 3D printing patterns, we can observe an increase in compressive modulus with printing patterns of decreased tortuosity. Thus, 90° scaffolds had the highest compressive modulus, followed by the 60° and the 45° printing patterns. As the structure is more tortuous, the evaporation of the solvent from the printed scaffolds is slower, reverberating in the cross-section definition that becomes less structured, and being detrimental to a proper compression response of the scaffolds.

Taking into consideration the mechanical properties and the capability to promote cell adhesion and proliferation of the fabricated dual-porosity scaffolds, we selected those with larger pores, printing patterns of 90° and 60° and initial GMS loadings of 40 % and 50 %. In those scaffolds, adhesion and proliferation were the highest; a property needed to obtain an efficient cell infiltration, population and, ultimately, tissue formation when relaying on micro-fracture techniques, where the initial percentage of hMSC populating the scaffold is very low [64]. Moreover, these printing patterns and compositions resulted in the highest compressive moduli and covered a broad range of mechanical properties, which will be useful to mimic the native zonal properties of cartilage.

The microstructure of the four selected dual-porosity 3D printed scaffolds was analyzed by micro-computed tomography (μCT), which revealed the average pore diameter, percentage of opened and closed porosity, pore surface density and connectivity density (Fig. 3C, D, E and Figure S11, Supplementary Information).

The total opened porosity was high for all selected structures with similar values of 83.4 ± 0.5 % and 83.3 ± 0.9 % for large pores_40 % scaffolds of 90° and 60° printing patterns, respectively, and 77.8 ± 0.6 % and 80.5 ± 0.2 % for scaffolds with 50 % GMS loading and 90° and 60° printing patterns, respectively (Fig. 3C, D and E). However, this value was not affected by the size of the structural pores as the fibers themselves already account for a very high porosity. In fact, the total porosity correlated well with theoretical values calculated using the gelatin/PLCL ratio in each scaffold composition and their densities, which disregarded the structural pores.

This calculation resulted in porosities of 83.4 % and 83.3 % (82.1 % theoretical microporosity) for scaffolds with 40 % GMS content and 90° and 60° printing patterns, and 77.8 % and 80.5 % (87.3 % theoretical value) for large pores_50 % scaffolds of 90° and 60° printing patterns, respectively (Fig. S11A, Supplementary Information).

The closed porosity measured in dual-porosity scaffolds was lower than 0.01 % for all patterns and compositions, which indicates high interconnectivity between the pores (defined by pore connections larger than 3 μm), essential for an efficient exchange of nutrients and wastes (Fig. S11B, Supplementary Information). In fact, the pore size measured by μCT revealed larger sizes than the ones measured by SEM images in the four scaffolds (47 μm), meaning that the high concentration of microspheres favours their association, resulting in larger pores (Figs. 1E and 3C). To corroborate this statement, the connectivity density was also measured, being a parameter that quantifies the number of connections between the different nodes in a scaffold per volume unit. A high interconnectivity is desired to facilitate cell infiltration and population. As expected, the interconnectivity density was significantly lower in the 40 % ($6.4{\cdot}10^3 \pm 0.2{\cdot}10^3$ mm^{-3} and $6.3{\cdot}10^3 \pm 0.3{\cdot}10^3$ mm^{-3} for 90° and 60° printing pattern scaffolds, respectively) than in the 50 % scaffolds ($11.5{\cdot}10^3 \pm 0.4{\cdot}10^3$ mm^{-3} and $10.0{\cdot}10^3 \pm 0.3{\cdot}10^3$ mm^{-3} for scaffolds with 90° and 60° printing patterns, respectively), due to the lower percentage of porogen that was included in the ink composition

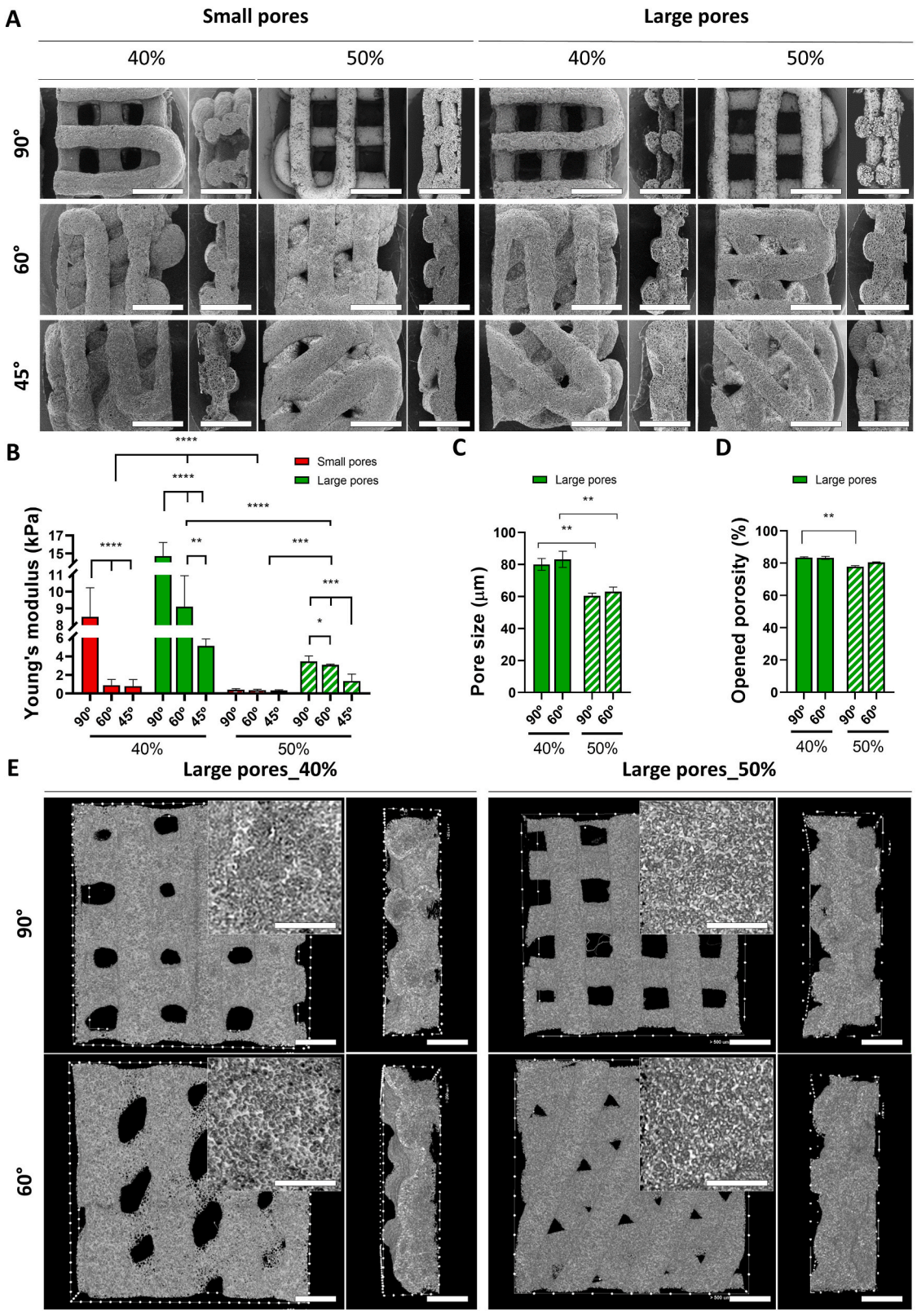

Fig. 3. Structural characterization of dual-porosity scaffolds with different composition and printing patterns. (A) SEM images of the top and cross-sectional views of the dual-porosity 3D printed scaffolds with printing patterns of 90°, 60°, and 45°. Scale bar is 2 mm in all the images. (B) Compressive moduli of dual-porosity scaffolds with different printing patterns and compositions. (C, D) Pore size (C) and total open porosity (D) in dual-porosity scaffolds with large pores, different initial GMS loading and with printing patterns of 90° and 60°, as measured from μCT analysis. (E) μCT images of top and cross-sectional views of dual-porosity scaffolds with large pores and different initial GMS loading and printing patterns. Scale bar in the top-view and cross-section images is 1 mm. and in the inset images is 500 μm. Insets show higher magnification images of the microporosity appearance. Error bars in B-D show standard deviation. Statistical significance of compressive modulus (n = 3), pore size and opened porosity (n = 2000) were calculated from two-way ANOVA with *posthoc* Tukey's multiple comparison tests; (****) $p < 0.0001$, (***) $p < 0.001$, (**) $p < 0.01$, and (*) $p < 0.1$ was used.

(Fig. S11B, Supplementary Information). The initial GMS loading also impacted the scaffold's pore surface densities with a lower pore surface area per volume ratio for scaffolds with lower porosity (Fig. S11B, Supplementary Information).

2.4. Structurally distinct dual-porosity 3D printed scaffolds steer hMSC differentiation towards different chondrogenic phenotypes

Having proved the impact of the different micro- and macro-structural properties of dual-porosity scaffolds on their mechanical and biological properties, we hypothesized that mimicking the cell proliferative activity and mechanical properties of the native tissue will result in the modulation of hMSC chondrogenic differentiation. We seeded hMSC on dual-porosity scaffolds and cultured them on basal and chondrogenic media conditions for 14 and 28 days, evaluating the impact on cell population, cell phenotype, deposition of characteristic ECM proteins and mechanical properties of the formed tissue (Table 1). We also promoted hMSC differentiation following the traditional pellet culture as the "gold-standard" for chondrogenesis and used it as a control.

After 28 days of culture, quantification of total DNA showed a higher cell number on scaffolds with a 60° printing pattern regardless of the fiber's internal porosity and the culture media conditions (Fig. 4A). Within the scaffolds with a 60° printing pattern, the number of cells increased with the culture time and in basal media (BM) as compared to chondrogenic media (CM) conditions. We ascribed this response to the less active differentiation process of hMSC cultured in BM as compared to cells cultured in CM conditions. The cell number also increased with the initial GMS loading, with scaffolds with 50 % loading accounting for $8.1{\cdot}10^5 \pm 0.6{\cdot}10^5$ and $15.4{\cdot}10^5 \pm 0.8{\cdot}10^5$ cells cultured in CM and BM conditions, respectively, as compared to $5.2{\cdot}10^5 \pm 0.4{\cdot}10^5$ and $6.9{\cdot}10^5 \pm 0.9{\cdot}10^5$ cells in scaffolds with 40 % initial GMS loading cultured in chondrogenic and basal media, respectively. hMSC differentiated in traditional pellet cultures showed a reduced cell proliferation as compared to cells cultured on large pore_50 % scaffolds and 60° printing pattern. The scaffolds with a 90° printing pattern showed a lower proliferation, having cell numbers that remained unvaried during the culture period and regardless of the culture media condition. These data were also confirmed by histological staining, where a higher amount of cells was visible (nuclei stained in black) in scaffolds printed with a 60° pattern (Fig. 4B). The cell density seems higher in the central area of the scaffolds, validating the hypothesis that a more tortuous scaffold structure with smaller structural pores can better retain seeded cells.

Glycosaminoglycans are cartilage-characteristic ECM molecules synthesized by chondrocytes and responsible for creating a negatively charged microenvironment, capable of entrapping a large amount of interstitial fluid and, hence, contributing importantly to the compressive mechanical properties of the tissue (Fig. 4E). The amount of deposited GAG in dual-porosity scaffolds was quantified after 28 days of culture in BM and CM conditions, as well as in gold-standard pellet culture controls (Fig. 4C). The amount of deposited GAG/DNA was not significantly different among the different groups in CM conditions, showing in all cases a high amount of total GAG ranging from 0.32 to 1.76 μg per scaffold (Fig. S12, Supplementary Information). Significant differences were only detected for hMSC cultured on BM conditions which, surprisingly, surpassed those of cells cultured on CM conditions. Specifically, the GAG/DNA ratio was significantly higher in the large pore_50 % than in the chondrogenic control. The opposite trend was observed in the scaffolds with 60° patterns, which exhibited high cell proliferation and lower synthesis of sulfated GAG. The presence of GAG in the scaffold was also analyzed by histological staining with Safranin-O, showing a more intense garnet color in the scaffolds with a 90° pattern (Fig. 4B).

Some studies have suggested that the use of the exogenous growth factor TGF-β can mask the effect of mechanical loading on the chondrogenic differentiation of stem cells. Thus, cell that are sensing a strain and are cultured in basal media without TGF-β, present a GAG/DNA deposition that is not significantly different from those culture under the same strain conditions with various concentrations of exogenous TGF-β1. Most interestingly, the synthesis of TGF-β3 was shown to be higher in samples were cells were cultured under strain but without the addition of exogenous TGF-β1 [65]. These results suggest that mechanical loading or cell culture under strain promotes chondrogenesis through the TGF-β pathway and it is somewhat hindered by the presence of the exogenous protein. Thus, our results may indicate that cells cultured on scaffolds with large pores and with a 90° printing pattern are sensing a cytoskeletal strain similar to a mechanical load. The cytoskeletal strain is translated into activation of the TGF-β pathway which is masked by the use of exogenous TGF-β in chondrogenic media conditions. In fact, it has also been shown that activation of TGF-β can occur through the activation of integrin pairs [66], which would support the idea that the topography present on dual-porosity scaffolds activates chondrogenic differentiation through the TGF-β pathway, although a more thorough investigation would be needed to verify this hypothesis. The genetic expression of proteoglycans such as aggrecan (*ACAN*) and versican (*VCAN*) was further evaluated by RT-PCR (Fig. 4F, Figure S13F, G, S15F and G, Supplementary Information). Aggrecan is a key contributor to the compressive properties of cartilage as chondroitin sulfate chains in its structure entrap high volumes of interstitial fluid. Versican, in contrast, has a lower amount of negatively charged groups resulting in a more fibrotic behaviour that aids in the support of the cells and remodelling of the ECM [1,67]. *ACAN* was downregulated in the majority of dual-porosity scaffolds except in scaffolds with large pores, 40 % initial GMS loading and 90° pattern cultured in CM after 14 days of culture. Similarly, *VCAN* was not significantly upregulated (less than 2-fold) in

Table 1
Summary of scaffold formulations and associated biological outcomes after 28 days in culture.

Large pores_50 %				Large pores_40 %			
50 % GMS loading				40 % GMS loading			
60°		90°		60°		90°	
BM	**CM**	**BM**	**CM**	**BM**	**CM**	**BM**	**CM**
High cell proliferation. Medium-high GAG deposition. Upregulated *COL2A1*, *SOX5*, *SOX9*. Downregulated *COL1A1*. Highly downregulated *COL10A1*.	Medium cell proliferation. Medium-high GAG deposition. Highly upregulated *COL2A1*, *SOX5*. Upregulated *SOX9*. Downregulated *COL1A1*. Highly downregulated *COL10A1*.	Low cell proliferation. High GAG deposition. Upregulated *COL2A1, SOX5, SOX9*. Downregulated *COL1A1*. Highly downregulated *COL10A1*.	Low cell proliferation. Medium-high GAG deposition. Highly upregulated *COL2A1*, *SOX5*. Upregulated *COL1A1*. Downregulated *SOX9*. Highly downregulated *COL10A1*.	Medium cell proliferation. Low GAG deposition. Highly upregulated *SOX5*. Upregulated *COL2A1*, SOX9. Downregulated *COL1A1*. Highly downregulated *COL10A1*.	Medium cell proliferation. Low GAG deposition. Highly upregulated *COL2A1*, *SOX5*. Upregulated *COL1A1*. Downregulated *SOX9*. Highly downregulated *COL10A1*.	Low cell proliferation. Medium-high GAG deposition. Highly upregulated *SOX5*. Upregulated *COL2A1*, *SOX9*. Downregulated *COL1A1*. Highly downregulated *COL10A1*.	Low cell proliferation. Low-medium GAG deposition. Highly upregulated *COL2A1*, *SOX5*, *SOX9*. Highly downregulated *COL1A1* and *COL10A1*.

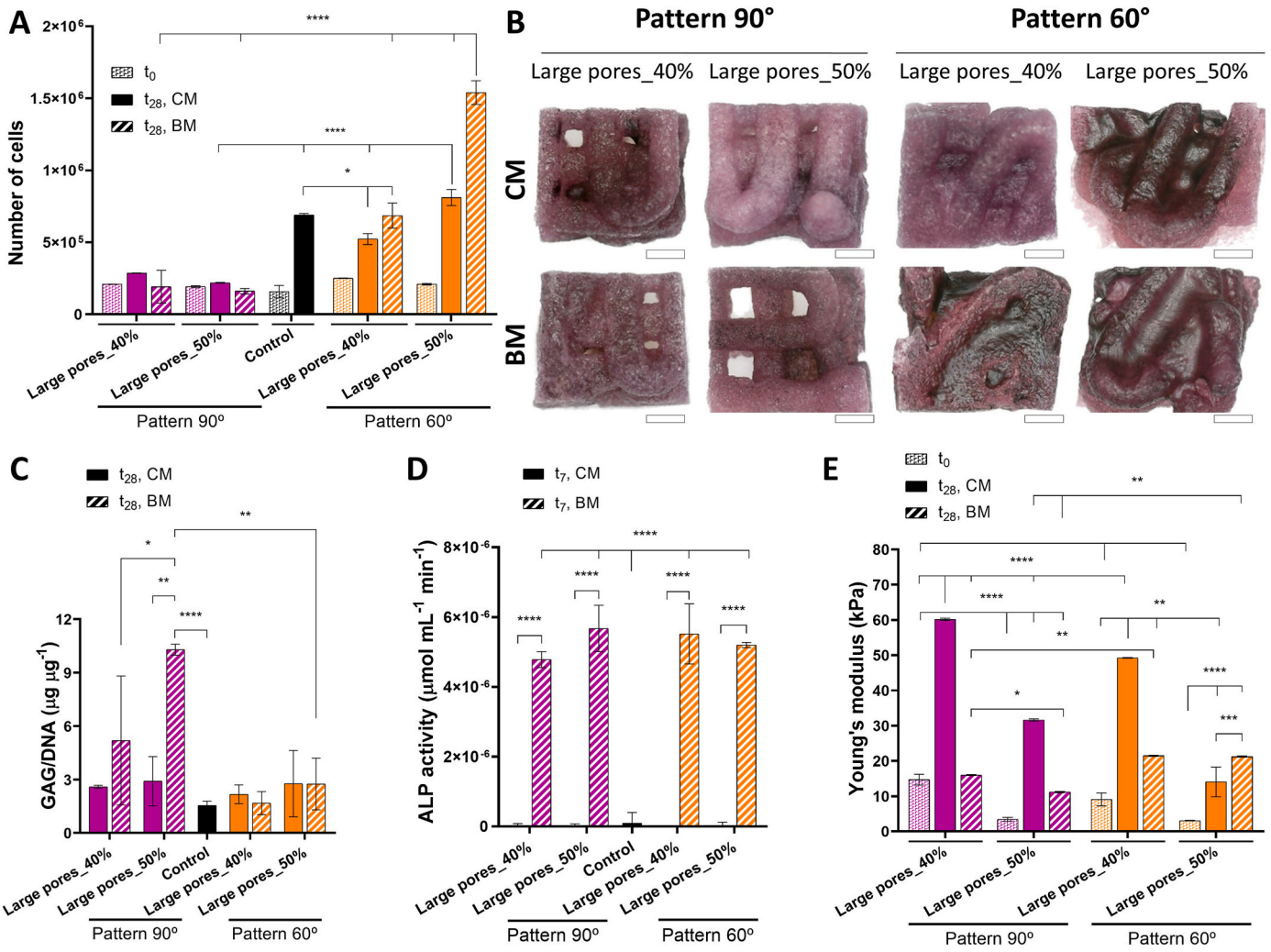

F

			t_{14}									t_{28}								
			COL1A1	COL2A1	COL10A1	RUNX2	BGLAP	ACAN	VCAN	SOX9	SOX5	COL1A1	COL2A1	COL10A1	RUNX2	BGLAP	ACAN	VCAN	SOX9	SOX5
Pattern 90°	Large pores 40%	CM	-1.3			5.3		2.5	2.3	7.3	10.8	-3.0	6.4	-3.6	2.1		-7.3	0.7	2.9	6.0
		BM	-4.1	0.9	-2.6	1.1	-1.8	-6.7	-3.1	-0.5	7.4	-2.1	2.8	-5.3	1.0	-0.9	-6.8	0.6	0.1	4.7
	Large pores 50%	CM	1.7	10.3	-4.0	2.0	-2.6	-3.4	0.3	0.6	4.2	1.1	9.9	-6.5	1.9	-1.7	-3.5	0.3	-0.8	4.7
		BM	-2.9	5.5	-3.0	1.8	0.1	-5.1	-0.2	0.3	5.8	-1.4	1.9	-4.8	1.0	-0.1	-7.0	0.9	0.5	2.6
Pattern 60°	Large pores 40%	CM	-2.3	7.6	-4.1	2.7	-1.4	-4.0	0.4	3.4	8.5	0.9	3.1	-6.4	2.4	-2.0	-5.9	-0.1	-1.9	5.1
		BM	-2.5	1.6	-3.8	2.8	-3.2	-5.4	-0.4	2.7	9.5	-0.9	1.1	-5.4	1.4	-0.4	-6.4	1.7	0.1	3.1
	Large pores 50%	CM	0.9	11.9	-6.7	2.2	-0.7	-1.0	0.5	1.9	5.9	-1.2	4.4	-6.2	2.4	-1.0	-3.0	-1.3	0.2	4.7
		BM	-1.0	2.0	-3.1	3.4	1.1	-1.8	-0.2	0.3	2.1	-0.7	1.6	-3.6	0.8	2.6	-2.4	0.1	0.5	1.4
	Control		1.1	12.8	-4.9	1.3	-0.5	0.2	0.5	2.3	5.2	0.5	10.2	-3.4	1.1	-0.5	-1.3	0.1	0.9	4.3

(caption on next page)

Fig. 4. Chondrogenic differentiation in dual-porosity scaffolds. (A) Number of cells as calculated from the DNA content in the dual-porosity scaffolds and control samples (pellet culture) after 28 days of culture in chondrogenic (CM) and basal media (BM). (B) Histological evaluation hMSC seeded dual-porosity constructs after 28 days of culture in CM (*top*) and BM (*bottom*) and stained for glycosaminoglycans (Safranin-O, garnet), cytoplasm (Fast Green, green) and nuclei (Weigert's Iron Hematoxylin, black). Scale bar in all the images is 1 mm. (C) DNA-normalized glycosaminoglycan (GAG) deposition by hMSC cultured for 28 days in dual-porosity scaffolds in CM and BM and control pellet cultures. (D) Alkaline phosphatase activity (ALP) of hMSC cultured for 7 days on dual-porosity scaffolds in CM and BM conditions and control pellets. (E) Compressive modulus of dual-porosity scaffolds before and after 28 days of culture with hMSC in CM and BM conditions. (F) Heat-map of the gene expression fold-increase values obtained from RT-PCR analysis of cells cultured in the scaffolds in CM and BM for 14 (left, t_{14}) and 28 days (right, t_{28}). Statistical significance of the number of cells, ALP activity, compressive modulus and DNA normalized GAG content ($n = 3$) were calculated from two-way ANOVA with *posthoc* Tukey's multiple comparison tests; (****) $p < 0.0001$, (***) $p < 0.001$, (**) $p < 0.01$, and (*) $p < 0.1$ was used. (For interpretation of the references to color in this figure legend, the reader is referred to the Web version of this article.)

any of the scaffolds, except those with large pores, 40 % initial GMS loading and 90° pattern after 14 days of culture in CM. The expression of *ACAN* and *VCAN* in these scaffolds was higher than the measured for the gold-standard pellet culture in CM, highlighting the potential of dual-porosity scaffolds to promote the formation of proteoglycan-rich cartilage.

One of the main difficulties in the differentiation of hMSC toward the chondrogenic lineage is to hinder the progression toward hypertrophic phenotypes. One characteristic early marker linked to the terminal differentiation of the cells is the ALP activity. Thus, we evaluated the release of ALP to the medium by hMSC cultured for 7 days on the different dual-porosity scaffolds under CM and BM conditions (Fig. 4D). As expected, hMSC cultured in BM, regardless of the scaffold architecture, showed an ALP release that ranged from $4.8{\cdot}10^{-6}$ to $5.7{\cdot}10^{-6}$ μmol mL^{-1} min^{-1}.

However, hMSC cultured on the different scaffolds on CM showed all an ALP release that was lower than that measured in the gold-standard pellet culture, although not significantly different. Again, this highlights the unique ability of dual-porosity scaffolds to drive a chondrogenic differentiation of hMSC cultured within.

To further evaluate the differentiation state of hMSC cultured on dual-porosity scaffolds, we analyzed the gene expression of characteristic chondrogenic and osteogenic (or hypertrophic) markers after 14 and 28 days of culture in CM and BM conditions (Fig. 4F, Figure S13, S14, **S13** and **S16**, Supplementary Information). These values were normalized to the relative expression of hMSC seeded in 2D surfaces and cultured in basal conditions (Fig. S17, Supplementary Information). *COL2A1* was upregulated during the first stages of hMSC differentiation (t_{14}) and slightly decreased after 28 days of culture in the scaffolds cultured in CM. This gene expression reduction upon the culture time may potentially result from ongoing protein synthesis. However, hMSC cultured on dual-porosity scaffolds with large pores, 50 % loading and a 90° pattern, sustained these high expression levels over time (10.3 ± 3.5 and 9.9 ± 2.4 fold at t_{14} and t_{28}, respectively), suggesting an extended and larger deposition of the protein. It is noteworthy that the expression of *COL2A1* for cells cultured on these scaffolds was similar to the one of pellet cultures, which also showed an extended expression of the chondrogenic marker (12.8 ± 2.0 and 10.2 ± 0.2 fold at short- and long-term culture, respectively). Contrary, for cells cultured on scaffolds with large pores, 40 % loading and the same 90° pattern, the expression of *COL2A1* was initially not detected but upregulated after 28 days of culture, probably indicating a delayed chondrogenic differentiation.

The expression of *COL1A1*, which is considered a marker of hypertrophy, was slightly upregulated in the first stages of differentiation in the scaffold with large pores and 50 % loading fabricated with a 90° printing pattern (1.7 ± 0.1 folds). We hypothesized this to be related to the lower roughness, and hence, higher cell spreading that cells can acquire on this scaffolds (Fig. 2A). Nevertheless, this upregulation was similar to that detected for hMSC in traditional pellet culture, showing a $\Delta\Delta C_t$ value of 1.1 ± 0.1. Interestingly, cells cultured on scaffolds with large pores, 40 % loading and a 60° pattern showed a marked upregulation of *COL2A1* (7.6 ± 0.1 folds), while displaying a downregulation of *COL1A1* (-2.3 ± 1.4). The calculated *COL2A1/COL1A1* expression ratio (Fig. S14 and S16) showed higher values for cells cultured in CM as compared to those in BM. The ratio was in all the cases high, and supported the idea of a later onset of chondrogenesis for cells cultured on samples with a 90° printing pattern. After 28 days of culture, the collagen II/collagen I expression ratio was approximately 650 and 400 for scaffolds with 40 % and 50 % loading and a 90° printing pattern, respectively; and 5 and 50 for the same scaffold composition but with a 60° printing pattern, respectively.

Another gene that is typically expressed in the hypertrophic maturation stage of the chondrocytes is *COL10A1*, which appeared to be downregulated after 14 and 28 days of culture, for cells cultured in all different dual-porosity scaffolds, as well as in control pellet cultures.

The expression of other transcription factors such as Sox9, Sox5 and RunX2 was also investigated as markers of chondrogenic differentiation. Sox5, Sox6 and Sox9, also known as the Sox trio, work together to activate the expression of *COL2A1* and have been traditionally considered as markers for chondrogenesis [68]. Contrary, the expression of *RUNX2* (RunX Family Transcription Factor 2) it is known to regulate mineralization through regulation of RANK and is therefore associated to an osteogenic differentiation. Nevertheless, RunX2 also plays a crucial role in the maturation of chondrocytes towards hypertrophic states present on the deep zone of cartilage and on the proliferation of chondrocytes of the middle zone via regulation of cell cycle genes such as Gpr132, Sfn, c-Myb, and Cyclin A1 [69]. Thus, expression of *RUNX2* during differentiation towards the specific phenotypes found in hyaline cartilage is expected. In dual-porosity scaffolds, *RUNX2* and *SOX9* appeared upregulated in the early steps of the differentiation when cells were cultured in CM, with a fold increase of 0.8–5.3. Furthermore, Sox5 is a transcription factor that acts together with the Sox9 protein during the development of the growth plate preventing premature cell differentiation and promoting the expression and deposition of collagen II.

Cells cultured in dual-porosity scaffolds, showed a pronounced upregulation of *SOX5*, especially after 14 days of culture with a fold-increase of 2.1–10.8.

Finally, the expression of other proteins characteristic of hypertrophic and osteogenic environments such as BGLAP (osteocalcin) was also analyzed. Osteocalcin is a protein synthesized by osteoblasts and involved in the ECM mineralization process. Cells cultured in dual-porosity scaffolds presented a slight downregulation of the *BGLAP* expression, which could be taken as an indication of a hindered, or at least delayed, hypertrophic process. Taking into account the overall downregulation of *COL10A1*, *COL1A1* and *BGLAP*, it appeared that the phenotype of cells cultured in dual-porosity scaffolds presented a stable chondrogenic differentiation and absence of clear terminal or hypertrophic differentiation, highlighting again the potential of these scaffolds.

To validate the hypothesis that culture of hMSC in dual-porosity scaffolds leads not only to the chondrogenic differentiation of the cells but also to the deposition of a coherent ECM characteristic of cartilage, constructs were analyzed after 28 days of culture via immunofluorescence. Collagen II was present in the ECM of all constructs, particularly in those cultured in CM conditions (Fig. 5A). Interestingly, the deposition of a fibrilar collagen II appeared to be more evident in the scaffolds with a 90° printing pattern, which presented higher compressive properties than the 60° constructs (Fig. 3B, Fig. S18 and S17, Supplementary Information). Surprisingly, the deposited collagen II in the 50 % GMS-loaded scaffolds displayed a more fibrillary structure than in the 40 %

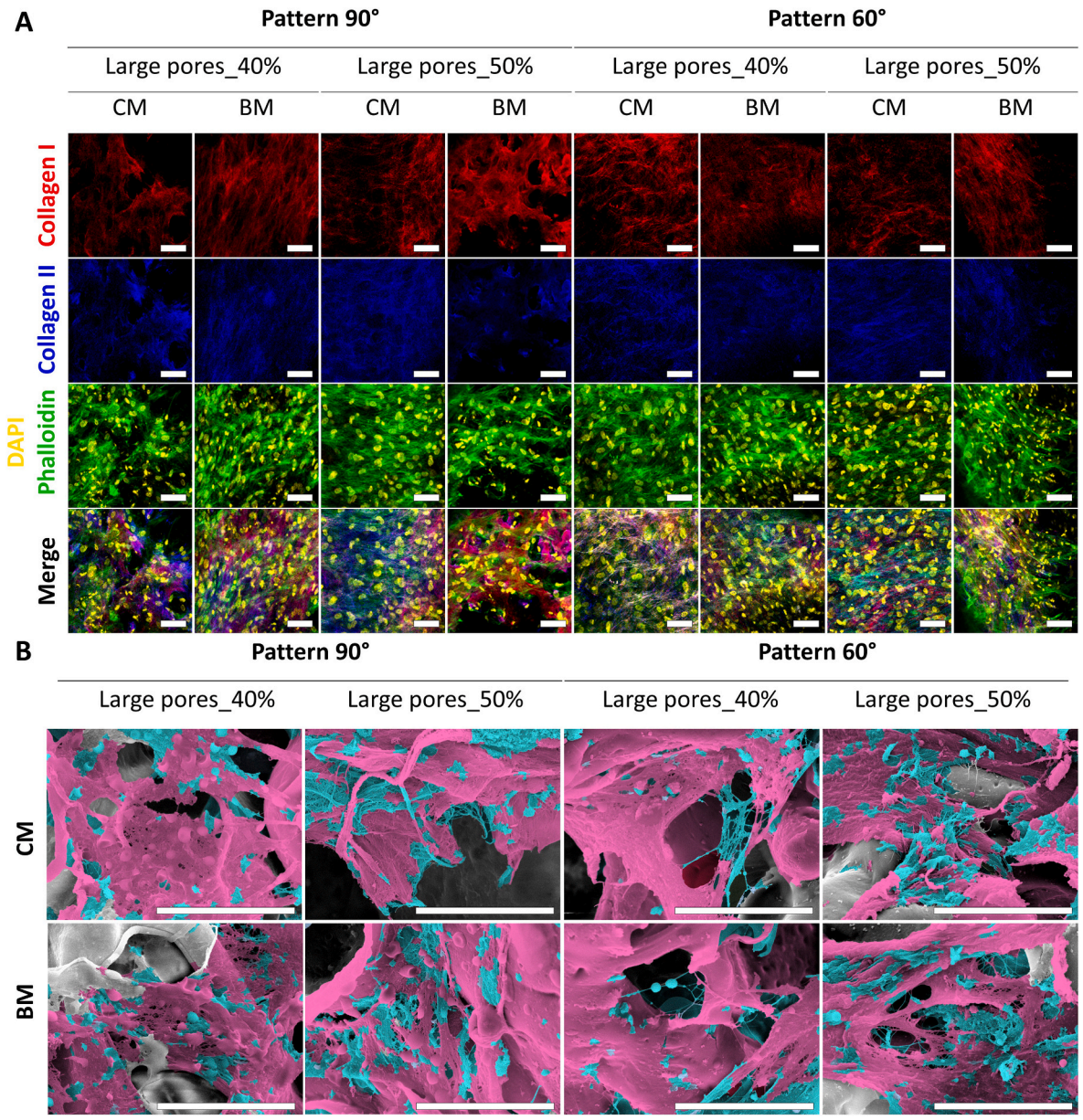

Fig. 5. ECM deposition in dual-porosity scaffolds. (A) Fluorescence microscopy images of hMSC cultured for 28 days on dual-porosity scaffolds and stained for collage I (red), collagen II (blue), DNA (yellow, nuclei), and F-actin (green). Scale bar is 100 μm in all images. (B) SEM images of hMSC-seeded dual-porosity scaffolds after 28 days of culture, showing a fibrillary ECM deposition (colored in blue) covering the surface of the constructs and the cell morphology (colored in pink). Scale bar is 30 μm in all the images. (For interpretation of the references to color in this figure legend, the reader is referred to the Web version of this article.)

composition, both cultured in chondrogenic conditions. In those scaffolds, we observed a higher pore surface density and better connectivity between them, which seems to drive the synthesis of a more consistent collagen II matrix (Fig. S11B, Supplementary Information). Contrary, the constructs cultured in BM exhibited a lower collagen II deposition and an increase in the production of collagen type I, highlighting the hypertrophic phenotype that was previously observed in these scaffold compositions. Especially, a higher collagen I deposition was observed on scaffolds with a 90° pattern cultured in BM as compared to the deposition of counterparts fabricated with a 60° pattern. Particularly, a more fibrous and organized collagen I matrix was evident in scaffolds with large pores and 40 % initial GMS loading with a 90° printing pattern, and in the 50 % scaffolds with a 60° pattern, both cultured for 28 days in BM. These scaffolds showed lower pore surface density and a decrease in the connectivity density between the micropores, which could have promoted cell differentiation towards a hypertrophic maturation stage (Fig. S11B, Supplementary Information).

The deposition of a consistent ECM was also analyzed by SEM imaging of dual-porosity scaffolds after 28 days of culture in CM and BM conditions (Fig. 5B and Fig. S19, Supplementary Information). A careful observation of the constructs revealed the presence of the cells and the formation of fibrillary structures covering the pores at the scaffold's fiber surface. Specifically, this organized matrix was more evident in scaffolds with large pores and 50 % loading cultured for 28 days in CM and BM, with both, 90° and 60° printing patterns. These scaffolds, in CM, exhibited an increased and more organized collagen II deposition in the immunostaining images and collagen I in BM (Fig. 5A). The ratio between collagen II and collagen I deposition and gene expression has been long considered as an indicator of the differentiation state of the cells [70,71]. We calculated the ratio of collagen II/collagen I deposition from fluorescence images (Fig. S18), what evidence a ratio above 1 for all scaffolds cultured in chondrogenic media (Fig. S20). Particularly,

scaffolds with a 90° printing pattern and 40 % and 50 % loading showed a collagen II/collagen I ratio well above 1.5. While the same compositions with a 60° printing pattern showed a ratio of around 1.

2.5. Multilayer dual-porosity 3D printed scaffold mimics the native cartilage and promotes the deposition of cartilaginous tissue

Previous studies have designed multilayer scaffolds aimed at cartilage regeneration based on the mechanical properties of the native cartilage, investigating the relationship between the compressive responses of said 3D printed scaffolds with different printing patterns [15]. Other studies have investigated the relationship between the mechanical properties of multilayer scaffolds and the fate of the seeded cells, demonstrating that mimicking the cartilage microenvironment can drive cell differentiation into specific phenotypes [19,28,58,72]. Here, we designed multilayered 3D printed scaffolds composed of dual-porosity scaffolds with different architectures that mimicked the natural hyaline cartilage's compressive properties and cellular phenotype.

The superficial layer of the native cartilage is characterized for displaying a fibrocartilage-like composition. Here, the cell density seems to be higher while the GAG concentration remained lower, resulting on the cartilage zone with the lowest mechanical properties. Chondrocytes have a persistent phenotype and an increased spread area and, collagen II, characteristic of hyaline cartilage, coexists with substantial amounts of collagen I [2,73–76]. Specifically, the coexistence of both proteins has been reported during development and maturation of the tissue, with concentrations of collagen I up to 10 % in the interstitial microenvironment [77]. The scaffolds with large pores, 50 % loading and 60° printing pattern were selected to recreate this cartilage zone due to its compressive properties and the cell phenotype and matrix deposition promoted. Briefly, this construct showed low glycosaminoglycan deposition (2.8 ± 1.9 μg $_{GAG} \cdot$ μg^{-1} $_{DNA}$), the highest cell number in CM ($8.1{\cdot}10^5 \pm 0.6{\cdot}10^5$ cells) and the lowest compressive modulus in CM (14.1 ± 4.2 kPa) (Fig. 4A–C, and E). In this scaffold type, the *COL10A1* gene expression was highly downregulated, meanwhile, the *COL1A1* and *COL2A1* genes were upregulated in the short term (Fig. 4F, Fig. S13 and S15, Supplementary Information). Further, the deposition of collagen I and II were visible in the immunostaining images forming an organized and fibrilar matrix (Fig. 5A and Figure S18, S20, Supplementary Information).

The middle zone of the cartilage accounts for a low cell density and a very active GAG synthesis, which leads to higher compression properties than in the superficial layer. Moreover, the only collagen present in this layer is type II, and the chondrocytes are in a proliferative stage of differentiation [2]. The scaffold composition that better fits these characteristics was the one with large pores, 50 % loading and a 90° printing pattern. This scaffold displayed a low cell number ($1.93{\cdot}10^5 \pm 0.07{\cdot}10^5$ cells), the highest GAG deposition in CM (2.9 ± 1.4 μg $_{GAG} \cdot$ μg^{-1} $_{DNA}$), and a high compressive modulus (31.6 ± 0.3 kPa) (Fig. 4A–C, and E). In these scaffolds, the *COL1A1* expression was downregulated, meanwhile, *COL2A1* was largely upregulated in both, the short- and long-term (Fig. 4F, Figure S13, S14, **S15** and **S16**, Supplementary Information). Interestingly, an abundant deposition of collagen type II was observed by immunofluorescence, forming a structured and fibrilar ECM (Fig. 5A, Fig. S18 and S19, Supplementary Information).

The deep zone of the natural cartilage is characterized by a very low cell density, which synthesizes a high amount of glycosaminoglycans. This structure is molecularly more similar to the subchondral bone layer, hence, this zone exhibits the highest mechanical properties of the tissue. Similarly, the ECM contains collagen X together with collagen II, highlighting the hypertrophic differentiation of the cells in this specific zone [2]. The scaffold with large pores, 40 % loading and a 90° printing pattern was selected to mimic the deep layer of the cartilage due to their bio-mechanical properties. In summary, this construct showed low GAG production (2.5 ± 0.1 μg $_{GAG} \cdot$ μg^{-1} $_{DNA}$), low cell density ($2.86{\cdot}10^5 \pm 0.02{\cdot}10^5$ cells), and the highest compressive modulus in chondrogenic conditions (60.2 ± 0.3 kPa) (Fig. 4A–C, and E). In this dual-porosity scaffold, the expression of *COL10A1* was higher than in the rest of the scaffolds while *COL2A1* was upregulated long-term (Fig. 4F, Fig. S13 and S15, Supplementary Information).

The three selected layers were printed consecutively to create a multilayer scaffold, changing ink between the deep and the middle zone and just the printing pattern between the middle and superficial layers. The multilayer scaffold was designed to be capable of mimicking the mechanical properties of the articular cartilage, supporting hMSC proliferation and driving their differentiation. The morphology of the fabricated scaffolds was evaluated by SEM, revealing that the 3D structure integrity of each layer was maintained (Fig. 6A). Analysis of the morphology shown in the top, middle and bottom layer and on the cross-section of the scaffold demonstrated an interconnected structure that enabled substantial cell proliferation (Fig. 6B). In fact, a higher proliferation (more than the 3-fold difference between single-layer and multilayer structures composed of 3 layers) was observed in the multilayer scaffolds compared with the individual layers that formed them. The cell number increased from $1.29{\cdot}10^6 \pm 0.07{\cdot}10^6$ cells in the individual layers (Fig. 4A) to $6.0{\cdot}10^6 \pm 0.9{\cdot}10^6$ cells in the multilayer scaffold after 28 days cultured in chondrogenic conditions (Fig. 6B). We hypothesized that despite having a vast amount of the cells being infiltrated inside the multilayer scaffold, some were adhered to the scaffold's surface which favoured their proliferation, as was shown by histological staining with Weigert's Iron Hematoxylin (Fig. 6E). Moreover, the multilayer scaffolds have a lower surface/volume ratio than the average of the individual 3D printed layers. This fact drives the seeding of a higher hMSC portion in the scaffold bulk than the surface, enhancing the cell-cell interactions that could increase the local concentration of growth factors and promote cell proliferation by autocrine and paracrine signaling.

Afterwards, we analyzed the deposition of characteristic matrix proteins in the multilayer scaffolds after 28 days of culture. An increase in the GAG deposition normalized to the DNA content was observed in the multilayer scaffold, reaching values of 15.4 ± 2.0 μg μg^{-1} (Fig. 6C), while the total GAG production in the individual dual-porosity scaffolds was almost halved (8.2 ± 3.4 μg μg^{-1}) as shown Fig. 4C. Moreover, the measured deposition of GAGs in the multilayer were higher than that reported in previous studies *in vitro* and similar to that obtained on in vivo studies [78–81]. The higher synthesis of GAG in the multilayer scaffold was also visualized by histological staining with Safranin O (Fig. 6E), as compared to the intensity of the garnet color with the same staining in the individual layers (Fig. 4B). We ascribed this response to the high amount of confined cells inside and within the fibers, on a now larger scaffold, that could have resulted in a hypoxic environment more similar to that found on the articular cartilage. Further, cell confinement within the pores could mimic the natural microenvironment of the chondron, leading to a more active differentiation and efficient GAG production that reach 11.7 ± 0.9 μg in the multilayer construct (Fig. S21, Supplementary Information).

The total collagen synthesis by the hMSC seeded in dual-porosity scaffolds was first evaluated by histological staining with Picrosirius red, which revealed the presence of collagen both in the scaffold surface and inside the fibers (Fig. 6F). To determine the specific collagen matrix being deposited in each scaffold zone, multilayer scaffolds were analyzed by immunofluorescence (Fig. 6G). The deposition of collagen II, the most abundant collagen type in the articular cartilage, was maintained constant throughout the three layers, highlighting the potential of the scaffolds as functional implants for cartilage regeneration. Interestingly, the collagen I deposition was gradual through the scaffold depth, with a decreased protein deposition towards the deepest layers of the multilayer scaffold, particularly in the hypertrophic zone as it occurs in the native tissue. The calculated collagen II/collagen I deposition ratio showed three very different scenarios with deposition ratios of approximately 1, 3 and 75 for the superficial, middle and deep layers of the scaffold, respectively (Fig. S22). In addition, collagen type X was

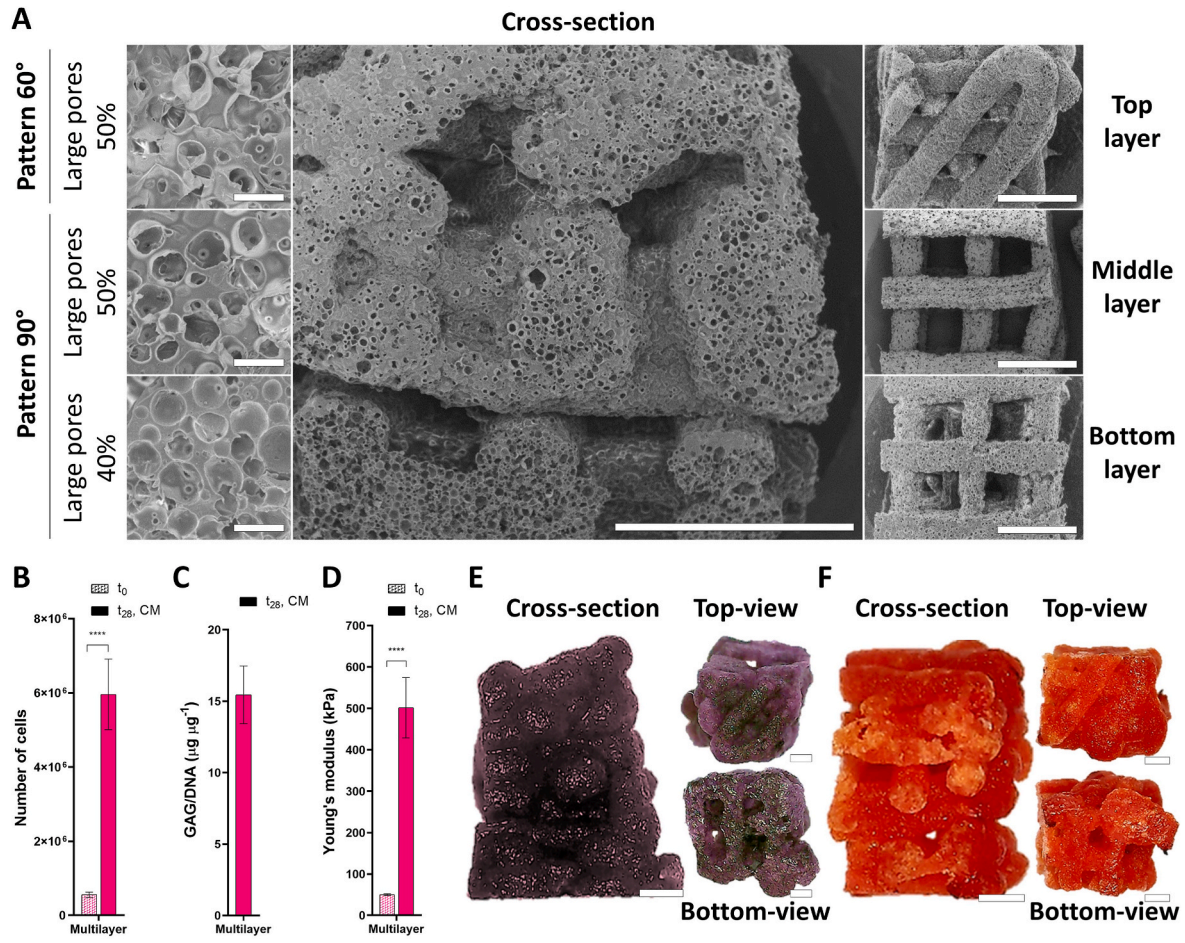

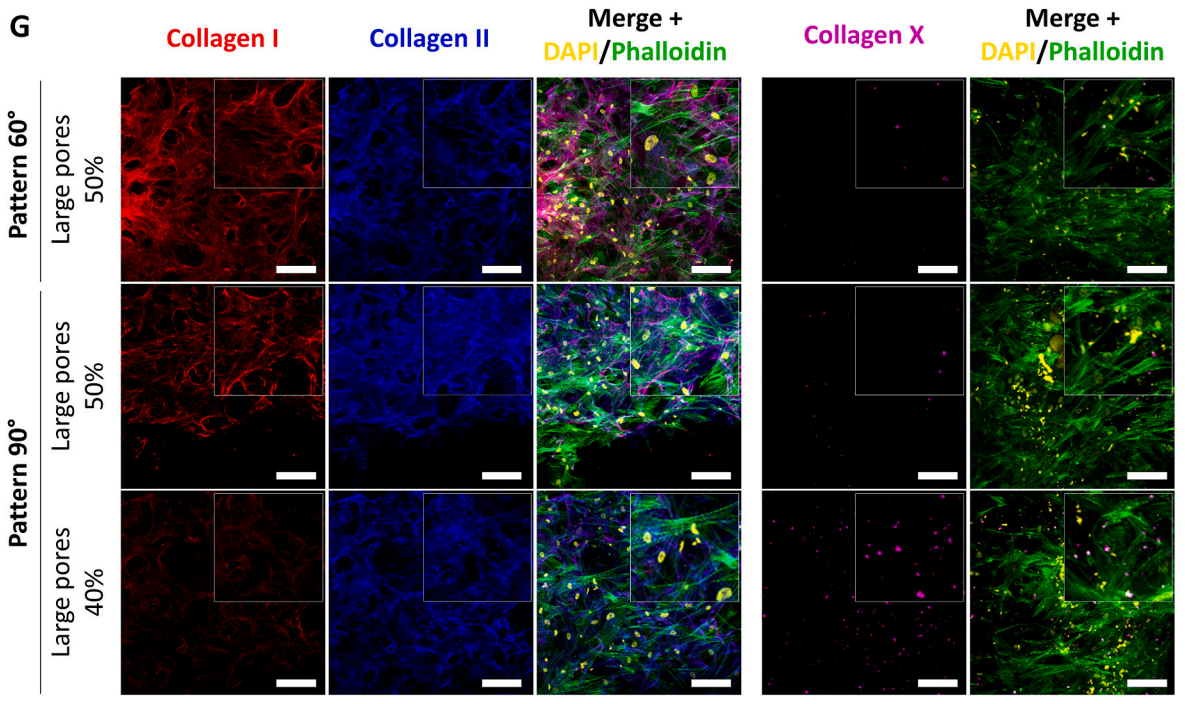

(caption on next page)

Fig. 6. Structural and biological characterization of multilayer dual-porosity scaffolds. (A) SEM images of the fiber surface (left, scale bar is 100 μm), cross-section (middle, scale bar is 2 mm) and top-, middle and bottom-view (right, scale bars are 2 mm) of the multilayer dual-porosity scaffold printing pattern. (B) Number of cells calculated from the DNA content in the multilayer dual-porosity scaffolds after 28 days of culture in chondrogenic media. (C) Deposition of GAG per DNA in the multilayer dual-porosity scaffolds after 28 days of culture in chondrogenic media. (D) Compressive moduli under compression of multilayer tissue construct after 28 days of culture. (E, F) Histological staining of multilayer dual-porosity scaffolds after 28 days of culture stained with (E) Safranin O (GAG, garnet), Fast Green (cytoplasm, green) and Weigert's Iron Hematoxylin (nuclei, black) and (F) with Picrosirius red (collagen, red). Scale bar is 1 mm. (G) Fluorescence microscopy images of hMSC cultured for 28 days on multilayer dual-porosity scaffolds and stained for DNA (yellow, nuclei), and F-actin (green), *(right panel)* collagen I (red), collagen II (blue) and *(left panel)* collagen X (violet). Scale bar is 100 μm in all the images. Inset size is 100 × 100 μm. Error bars show average ± standard deviation. Statistical significance of the number of cells, compressive modulus and normalized GAG content (n = 3) were calculated from one-way ANOVA with *posthoc* Tukey's multiple comparison tests; (****) $p < 0.0001$, (***) $p < 0.001$, (**) $p < 0.01$, and (*) $p < 0.1$ was used. (For interpretation of the references to color in this figure legend, the reader is referred to the Web version of this article.)

deposited in the deepest zone of the scaffold, mimicking the native ECM composition of this cartilage layer. Contrary, collagen X deposits were minimal in the superficial and middle layers (Fig. 6G).

The deposition of collagen II and I appeared as a fibrillar matrix but lacked the characteristic arcade-like orientation found on the native tissue. In accordance to the state of the art literature, the alignment of collagen fibers in cartilage development is a cell-independent process that occurs as a consequence of the application of loads to the tissue during skeletal development [82]. Thus, the formation of a phenotypically coherent and ECM-specific multilayered tissue construct like the one observed here, could be an ideal template for post-implantation tissue maturation.

The mechanical properties of the scaffolds are expected to increase as new tissue is being formed within. Thus, we analyzed compressive moduli of the cell-laden multilayer scaffold after hMSC seeding and after 28 days of culture in chondrogenic media. The modulus of the multilayer scaffold right after cell seeding reached values of 50.0 ± 2.2 kPa (Fig. 6D). An increase in the compressive properties of the multilayer scaffold as compared to those of the individual layers shown in Fig. 4E (21.2 ± 2.2 kPa) was clear. We hypothesized that the increased number of layers enhanced the construct's resistance to the compression, due to an increase number of interfaces.

After 28 days of chondrogenic differentiation, we observed an increase in the mechanical properties of the cell-laden multilayer scaffold of 5-folds (501.5 ± 72.7 kPa) as compared to the three individual constructs after cell culture under compression (105.9 ± 4.8 kPa) shown in Figs. 4E and 6D. Aside from the increase in the number of strands in the multilayer TE scaffold, the higher amount of glycosaminoglycans synthesized by the cells could be responsible for that mechanical response (Fig. 6C and Fig. S21, Supplementary Information). Interestingly, the compressive modulus of the cell-laden multilayer scaffold exhibited a similar value to the apparent compressive modulus for full-thickness cartilage, which has been reported to be of 380 ± 120 kPa [60]. Thus, we believe that dual-porosity multilayer scaffold could improve the outcomes of hyaline cartilage repair surgeries when in combination with microfracture techniques. Dual-porosity scaffolds would facilitate the accommodation of the exudated hMSCs, enable high cell proliferation and scaffold infiltration, and promote the deposition of layer-specific ECM components. The formation of an initial template with phenotypically coherent cells and a zone-specific matrix could provide a more durable implant permissive of the formation of mature and functional articular cartilage. Thereby, our manufactured scaffold appears as an innovative alternative that improves the proliferation rate and the cell differentiation parameters of previous studies using elastic but smooth 3D printed scaffolds. Specifically, some of these smooth constructs exhibited a low seeding efficiency (up to 20 %), which increased until 50 % after coating with human vitronectin. Moreover, slower proliferation ratios with low the cell numbers are usually obtained even after 14 and 28 days of culture. Gene expression after 28 days of some hypertrophic markers such as COL1A1 and COL10A1 tend to appear upregulated, while SOX9 expression apperas downregulated, highlighting that non-porous scaffolds are not able to drive and maintain a stable chondrogenic phenotype [13]. Although other authors increased the seeding efficiency ratios that also incremented the cell number and the matrix deposition after 14 and 28 days in basal and chondrogenic conditions, COL1A1 gene expression keeps appearing highly upregulated [14]. Instead, our 3D printed dual-porosity scaffolds displayed the capacity to control the gene expression of known cartilage hypertrophic markers such as COL1A1 and COL10A1 in each layer, contrary to other smooth multilayer scaffolds where up to 6- and 70-fold upregulation of COL1A1 and COL10A1 is visible, respectively [58].

3. Conclusions

Altogether, we manufactured a large library of 3D printed scaffolds using composite inks based on the mixture of 13 μm, 24 μm, or 47 μm diameter gelatine microspheres with poly-(*L*)-lactide-co-caprolactone at 20, 30, 40 and 50 % loading. Particle diameter and loading had impacted the rheological properties of the inks and, thus, into the ink printability and scaffold printing error. Inks prepared with particle diameters of 13 μm at the lowest loading and particles of 24 μm diameter clogged at the printer needle and resulted non-extrudable, and inks with 40 % and 50 % particle loading (13 μm and 47 μm diameter) had the smallest printing error. After lixiviation, the in-fiber pore size and the surface area/volume ratio of the 3D structures presented radical differences that allowed the control of adhesion and proliferation of human mesenchymal stem cells. Cells cultured on structures with small pores (13 μm GMS) presented a lower projected surface area than cells adhered to structures with larger pores (47 μm GMS) and higher initial GMS loading of 50 % led to higher proliferation. Structures printed following different patterns (90°, 60° and 45°) enable further control over the mechanical properties of the structures, with higher mechanical properties measured in scaffolds with higher initial particle diameter and lowest loading of 40 %. Analysis of the interplay between the used 3D printing pattern (or mechanical properties) and the percentage of porogen loading on chondrogenic cell differentiation revealed that the least tortuous patterns of 90° promote more active differentiation processes that resulted in lower proliferation rates but higher deposition of extracellular matrix components characteristic of cartilage, such as collagen II and glycosaminoglycans. Contrary, more complex 3D printing patterns steered cell differentiation towards earlier differentiation stages, such as those observed in the superficial zone of the natural tissue. Multilayer scaffolds were designed to mimic the mechanical properties and to steer stem cell differentiation to the characteristic chondrogenic phenotypes. Fabrication was done in a continuous process in which the inks were changed between the layers. The proliferation rate and the glycosaminoglycan deposition increased dramatically in multilayer dual-porosity scaffolds as compared to the individual layers, showing an influence of these parameters with the construct surface/volume ratio. The manufactured multilayer scaffolds promoted the deposition of collagen II homogeneously across the different zones, while the collagen I deposition was gradual, with a higher amount of protein in the superficial layer and lowest in the deep zone. These results suggest that the manufactured multilayer 3D printed scaffold in combination with microfracture techniques could improve the regeneration of osteochondral defects in a functional manner, promoting the deposition of layer-specific ECM proteins and promoting a layer-specific chondrocyte phenotype. Yet, further in vivo experimentation in

chondral defect models as well as long-term safety of the scaffolds would be needed to validate these results. In conclusion, these results highlight the importance of the careful design of the compressive properties and the structural and in-fiber porosity parameters to enhance the deposition of cartilaginous tissue by mimicking the native cartilage microenvironment.

4. Experimental section

Materials: Poly-(*L*)-lactide-co-caprolactone, having an inherent viscosity of 5.1 dL/g (PURASORB PLC 7038 B) and a 70/38 L-lactide to caprolactone monomer ratio, was purchased from Corbion (Gorinchem, The Netherlands).

Synthesis and characterisation of gelatine microspheres: Gelatine microspheres of different diameters were prepared by emulsion of a gelatine (type A from porcin skin, 410875000, 110–130 Bloom, Thermo Fisher Scientific) solution at 10 %, 20 % or 30 % (w/v) concentration in distilled water into a liquid paraffin oil (Sigma-Aldrich) bath at an addition rate of 0.5 mL s^{-1}. Span 80 (Sigma-Aldrich) was added to the paraffin bath as a surfactant at a 1:100 (v/v) surfactant/oil ratio. The initial gelatin solution/oil ratio was 1:5 (v/v) for all emulsions. After the complete addition of the gelatin solution, the round bottom flask containing the mixture was transferred to an oil bath preheated to 50 °C and emulsified under mechanical stirring at 500 rpm for 15 min. Thereafter, the flask was transferred to the fridge at 4 °C and allowed to cool down for 30 min to stabilise the formed particles (induction of gelation). The particle emulsion was then broken by adding acetone at a 1:4 (v/v) acetone/emulsion ratio. The GMS were recovered by vacuum filtration using a Whatman n°1 filter paper and the remaining oil was removed by rinsing with acetone. The recovered particles were then let air-dry for at least 24 h.

Particle diameter was characterized by optical and scanning electron microscopies. The GMS diameter was measured from the SEM images, taking 150 measurements of each sample. Standardization of the protocol of GMS synthesis was done by creating three batches of the different concentrations and a large-scale batch, comparing the diameters obtained (Fig. S2 and S3, Supplementary Information).

Formulation and rheological characterization of composite inks: A 20 % (w/v) solution of PLCL in 1,4-dioxane (Scharlau) was prepared by dissolving the polymer at 60 °C for 24 h under vigorous stirring. Afterwards, the clear solution was let cool down to room temperature and the GMS were mixed manually with a spatula at 20 %, 30 %, 40 %, or 50 % (w/v) ratios, obtaining the composite inks. Each composite ink (500 mg) was preheated in the oven at 25 °C for 5 min and then placed with a spatula in the bottom plate of the rheometer. Finally, the gap distance between the parallel plates was set to 650 μm. Prior to measuring the rheological properties, an oscillation amplitude test was done from 0.1 % to 10.0 % strain to determine the linear region of the deformation of the composite inks at 1.0 Hz and 25 °C. Subsequently, to characterize the viscoelastic properties of the composite inks under dynamic oscillation, the viscosity (η), storage (G') and loss (G'') moduli were analyzed over frequency scan (from 15.0 to 0.01 Hz) at 25 °C on an ARES-G2 rheometer (TA Instruments) using 20 mm parallel plates (stainless steel Peltier plate), and compared with a bare 20 % (w/v) solution of PLCL in dioxane as control. The fixed strain was subtracted, from the oscillation amplitude test. Afterwards, the behaviour of the composite inks under shear forces was measured to evaluate their rheological response during the printing process. The η and stress (σ) was then determined over a shear rate scan from 0.1 s^{-1} to 1000.0 s^{-1} at 25 °C.

Manufacture of 3D printed composite scaffolds, determination of 3D printing error and evaluation of the internal structure: The composite inks were extruded by 3D printing with a pressure-driven 3D Bioplotter system (EnvisionTEC), with 90°, 60° and 45° printing patterns, a fiber spacing of 800 μm, and a layer thickness of 200 μm to fabricate 10 x 10 × 2 mm scaffolds. The extrusion was performed with a G21 needle (800 μm of internal diameter) at 3.0–5.0 bar of pressure and 6.0–10.0 mm s^{-1} of extrusion speed at 25 °C. The dioxane in the scaffolds was left air-dry for 1 day prior to use. The scaffolds were characterized by SEM imaging as indicated below to evaluate the shape fidelity and the 3D printing error, using Equation (1).

$$\varepsilon_{\phi}\% = \frac{\phi_t - \phi_r}{\phi_t} \cdot 100$$

where $\varepsilon_{\phi}\%$ is the printing error of the diameter of the fibers, ϕ_t is the theoretical diameter of the fibers on the 3D model and ϕ_r is the experimental diameter of the fibers as measured from SEM images.

The multilayer scaffolds were manufactured using the parameters described above and using two different composite inks: 40 % and 50 % (w/v) GMS with 47 μm diameter in PLCL. To do so, 40 % (w/v) 47 μm GMS in PLCL were printed with a 90° printing pattern and let air-dry at least 30 min before the next ink (50 % (w/v) 47 μm GMS in PLCL with 90° printing pattern) was consecutively printed on top. After the drying process of the second layer, the same was executed with the 50 % (w/v) 47 μm GMS in PLCL ink, using a 60° printing pattern. The alignment between different layers in the xy- and z-axis was maintained by employing the Needle Calibration Station of the 3D Bioplotter System and configuring the number of layers by the VisualMachines Software. Each ink was extruded to manufacture scaffolds with 5-layer strands, obtaining multilayer scaffolds of approximately 10 x 10 × 6 mm.

Manufacture of non-porous 3D printed scaffolds: As control, non-porous scaffolds were fabricated using fused deposition 3D printing with a 3D NX Pro DUAL (Tumaker) and Simplify 3D as software to design the scaffold. Thus, we employed a 90° printing pattern, a percentage of filling of 50 % and 0.15 mm of onset to fabricate 10 x 10 × 2 mm scaffolds. For the PLCL melting, the cartridge, tip and bed temperatures were set into 220 °C, 250 °C and 55 °C, respectively. The extrusion was performed with a metallic G21 tip (800 μm of internal diameter) at 85 value of flow, a 3 value of extrusion multiplier and 1.3 mm s^{-1} of extrusion speed.

Leaching of Gelatine Microspheres and evaluation of microporosity: To leach the GMS from the dried 3D printed composite scaffolds, 3 samples of 4 x 4 × 2 mm were immersed in distilled water (30 mL) at 40 °C and left under stirring at 400 rpm. To define the time required to lixiviate the GMS from the scaffolds completely, elemental analysis was carried out at different time points using a TruSpec Micro CHNS microanalyzer (LECO Corporation) (Table S1, Supplementary Information). Composite scaffolds (1–2 mg) before and after leaching were used to determine the remaining quantity of elemental nitrogen (related to the gelatine presence). Time points of 1, 2, 4 and 7 days of leaching were used. Sulfamethazine (%C = 51,78,%H = 5,07,%N = 20,13,%S = 11,52) was used as a standard for the calibration and verification of the system stability, and the analysis was performed under O_2 at 1000 °C.

The size of the microporosity in dual-porosity scaffolds was evaluated from SEM images of the scaffold's fiber cross-section.

Micro-computerized tomography: The porous structure of the scaffolds was evaluated by micro-computed tomography using a SkyScan 1272 (Bruker; Kontich, Belgium). Samples (approximately 10 x 10 × 2 mm) were scanned at 50 kV voltage and 200 μA current, using an exposure time of 350 ms, a rotation step of 0.2°, a pixel size of 3 μm, and no filter. Subsequent reconstruction of the acquired tomograms and structural analysis were carried out using NRecon and CTAn software (Bruker), respectively. Prior to analysis, the scanned object volumes were converted into binary images using a threshold of 89–255.

Culture of Mesenchymal Stem Cells: Human mesenchymal stem cells were purchased from StemCell Technologies (Donor 2111410009, male, 56 years old) in passage 0. hMSC were expanded in monolayer culture at a density of $3.3 \cdot 10^3$ cells cm^{-2} using α-MEM (Gibco) culture media supplemented with 10 % (v/v) of fetal bovine serum (FBS, Corning) until 80 % of confluence. All experiments were performed at passage 4.

For chondrogenic differentiation in pellets, hMSC after trypsinization were resuspended in complete media at $8 \cdot 10^6$ cells mL^{-1}. Cell

dispersion (31.25 μL, $2.5{\cdot}10^5$ cells) were placed into a 15 mL centrifugation tube and centrifuged at 500 rcf for 5 min, forming a pellet in the bottom of the tube. The remaining media was removed and CM (500 μL) was added. The CM was composed of high glucose (4.5 mg mL^{-1}) DMEM (Dubelcco's Modified Eagle Medium, Gibco) with 100 μg mL^{-1} of sodium pyruvate (Gibco), 0.2 mM L-ascorbic acid-2-phosphate (ASAP, Sigma-Aldrich), 1 % 100x ITS liquid media supplement (Thermo Fisher Scientific), 40 μg mL^{-1} proline (Sigma-Aldrich), 100 U mL^{-1} penicillin/streptomycin (P/S), and 100 nM dexamethasone (Sigma-Aldrich). To the complete media and right before addition to the cultures, 0.01 μg mL^{-1} of TGF-β1 was supplemented (Peprotech). Media for both maintenance and differentiation conditions were changed every second day.

For cell culture on dual-porosity scaffolds and multilayer samples, the scaffolds were cut in pieces of approximately 4 x 4 × 2 mm using a surgical scalpel blade. The scaffolds were sterilized by immersion in a 70 % (v/v) ethanol solution for 20 min and rinsed 3 times with phosphate buffer saline (DPBS, Corning). The scaffolds were then placed into non-adherent 24-well plates. Cells after trypsinization were resuspended in BM at $8{\cdot}10^6$ cell mL^{-1}. Cell dispersion (25 μL, $2{\cdot}10^5$ cells) was seeded on top of each dual-porosity, and cell dispersion (75 μL, $6{\cdot}10^5$ cells) was seeded on top of each multilayer scaffold, and incubated for 2 h at 37 °C and 5 % CO_2. To obtain a homogeneous distribution of the cells through the scaffold height, the seeded scaffolds were flipped after the initial 2 h of incubation period and incubated 2 more hours upside down. For cell adhesion and proliferation experiments in the scaffolds, BM (500 μL) (α-MEM + 10 % (v/v) FBS + 1 % (v/v) ASAP + 1 % (v/v) P/S) was added to each scaffold, changing the culture media each 2–3 days. The scaffolds were collected after 3 and 21 days to analyze cell morphology and proliferation.

For the hMSC differentiation experiment, BM or CM (500 μL) was added to each scaffold as corresponding, changing the culture media every 2–3 days.

For the seeding of hMSC on multilayer scaffolds, CM (1.5 mL) was added to each sample changing the culture media every 2–3 days.

DNA quantification: Cells on dual-porosity scaffolds were washed 3 times with DPBS, placed in 1.5 mL centrifugation tubes and submerged into 1 mg mL^{-1} Proteinase K (300 μL) (Fisher BioReagents) solution in Tris/EDTA buffer (pH 7.6). The scaffolds were freeze-thaw 3 times using liquid nitrogen and digested overnight at 65 °C under stirring using a thermoshaker device (Grant Instruments). CyQuant Cell Proliferation Assay Kit (Thermo Fisher Scientific) was used to quantify the DNA content on each scaffold following the manufacturer's protocol. DNA was quantified by fluorescence analysis at 480 nm excitation and emission of 520 nm on a BioTek Synergy Neo2 Hybrid Multimode Reader (Agilent). The number of cells per scaffold was calculated assuming $6.6{\cdot}10^{-6}$ μg of DNA per cell.

Immunofluorescence: Cells on scaffolds were fixed with a 4 % paraformaldehyde (PFA, Thermo Fisher Scientific) solution in PBS for 20 min and rinsed three times with DPBS. For the proliferation experiment, cells were stained with a 1:500 solution of 1 mg mL^{-1} Hoechst-33342 (1:500, H1399, Invitrogen) in PBS for 15 min at RT to label cell nuclei of the cells, washing them 3 times with PBS. The cells were permeabilized with a 0.1 % TritonX-100 solution in PBS for 15 min and rinsed with PBS three times. The F-actin fibers were stained with Phalloidin-633 (1:400, A22284, Invitrogen) in PBS for 15 min at RT and washed three times in PBS. The stained samples were visualized using an Eclipse Ti2 Inverted Microscope (Nikon) equipped with an LED-based Lumencor Spectra II Illuminator and a large field Photometrics Iris 15 sCMOS camera, in epifluorescence mode at magnifications of 4x, 10x and 20x. For the hMSC differentiation experiment on scaffolds, after fixation and trypsinization the samples were blocked with a solution of 3 % (v/v) bovine serum albumin (BSA) and 0.01 % (v/v) TritonX-100 (Fisher BioReagents)) in PBS for 1 h at RT, and rinsed them 3 times with a solution of 0.3 % (v/v) BSA, 0.001 % (v/v) TritonX-100) in PBS. Samples stained for collagen I and II were incubated with 1:150 rabbit anti-collagen II antibody (ab34712, Abcam) for 1 h at RT and 1:200 goat anti-rabbit-647 secondary antibody (PA5-16891, Invitrogen) solution for 1 h at RT. Collagen I was stained with 1:100 anti-collagen I-488 antibody (ab275996, Abcam) for 2 h at RT. For collagen X stained samples, the cell-loaded scaffolds were incubated with 1:100 mouse anti-collagen X antibody (ab2573018, ThermoFisher) for 1 h at RT and 1:100 goat anti-mouse-488 secondary antibody (ab150113, Abcam) solution for 1 h at RT. The cytoskeleton and DNA were stained with 1:100 Phalloidin-568 (A12380, Invitrogen) for 2 h at RT and 1:500 Hoechst-33342 for 15 min at RT, respectively. The stained samples were visualized using a Light Scanning Microscope 880 Airyscan (Zeiss) equipped with Ar, DPSS and HeNe lasers, and PMT photomultiplier and GaAsP detector.

Collagen II/Collagen I immunostaining ratio quantification: To quantify the ratio between areas covered by collagen type II and I in immunofluorescence images, ImageJ software was used. Individual images of each channel were digitally processed adjusting the color threshold parameters to hue (0–255), saturation (0–255), brightness (100–255) (Fig. S18, Supplementary Information). The resulting areas were measured and the ratio was calculated.

Scanning Electron Microscopy: To visualise GMS, 3D printed scaffolds and the morphology of hMSC on top of the scaffolds, a SEM TM3030Plus was used (Hitachi High-Technologies).

Samples of GMS for SEM were prepared by dispersing GMS in acetone and casting a drop on top of a 12.5 mm diameter aluminium holder covered with a double-side carbon tape (9 mm diameter, PELCO Tabs, Ted Pella, Inc.). The acetone was left air-dry for 1 h prior to use. The scaffold samples for SEM were cut with a razor blade in the longitudinal and transversal directions and placed on an aluminium holder coated with double-sided carbon tape. Biological samples were fixed with a 4 % PFA solution in PBS for 20 min, washed 3 times with DPBS and dehydrated for 15 min in an ethanol dilution series in PBS with increasing concentrations (50 %, 70 %, 80 %, 90 %, 96 % and 100 %). Finally, the samples were incubated for 15 min in hexamethyldisilazane (HMDS, Thermo Fisher Scientific) and let air dry overnight in the chemical hood. The samples were placed into SEM aluminium holders. All samples after mounting were sputter coated with gold on a SC7620 Mini Sputter Coater/Glow Discharge System (Quorum) under Ar atmosphere (100 μbar), at 18 mA for 30 s and were imaged at 15 keV on backscattered electron mode.

GAG quantification: The deposited GAG after 28 days of hMSC culture on dual-porosity scaffolds were calculated with the DMMB assy. In brief, the solutions obtained after digestion with proteinase K (25 μL) (see details in the DNA assay) were collected and placed in triplicate in a 96-well plate. In each well, 5 μL of 2.3 M sodium chloride solution (to avoid the interference of genetic material in the measurements) and 150 μL of 1,9-dimethylmethylene blue (DMMB, 341088, Sigma-Aldrich) solution (pH 3.0) were added. A serial dilutions of chondroitin sulfate from shark cartilage (C4384, Sigma-Aldrich) solution in distilled water (10.0, 8.0, 6.0, 5.0, 4.0, 3.0, 2.0, 1.0 and 0.0 μg mL^{-1}) were prepared as standard curve and treated as above for the samples. The absorbances of the samples at 595 nm and 525 nm were measured with a BioTek Synergy Neo2 Hybrid Multimode Reader (Agilent) and the GAG content value of each sample was obtained by subtracting the first value from the second one and employing the standard to determine the GAG concentration on the samples.

Histology: After 28 days of culture, the scaffolds seeded with hMSC were fixed with a 4 % PFA solution in PBS for 20 min and rinsed 3 times with DPBS.

Samples for Safranin O were treated with Fast Green (Thermo Fisher Scientific), Safranin O (Sigma-Aldrich), and Weigert's Iron Hematoxylin to stain the GAG in garnet, the cytoplasm in green, and the nuclei in black. In brief, the scaffolds were stained on a series of solutions as follows: Weigert's Iron Hematoxylin staining (10 min), running tap water (10 min), 0.05 % (w/v) Fast Green in distilled water (5 min), 1 % (v/v) acetic acid in distilled water (10 s), 0.1 % (w/v) Safranin O in distilled water (5 min), and wash 3 times in PBS. The Weigert's Iron Hematoxylin staining solution was prepared fresh by mixing equal

volumes of stock solution A (1 % (w/v) Hematoxylin in 95 % (v/v) ethanol solution) with stock solution B (contains $FeCl_3$). The stained samples were imaged using a USB Digital Microscope (Bysameyee).

Samples for Picrosirius red were stained with a 0.1 % (w/v) Direct Red 8025G (Sirius red) solution in a saturated picric acid aqueous solution (1.3 % (w/v)) for 1 h, followed by two washing steps in acidified water (0.525 % (w/v) acetic acid in distilled water). Samples were dried with a Whatman No. 1 filter paper to prevent fading of the staining with the remaining acidified water.

Gene expression analysis: After 14 and 28 days of culture in BM and CM, hMSC on scaffolds were rinsed 3 times with DPBS. Scaffolds were immersed in TRIzol (1 mL) (Thermo Fisher Scientific) for 5 min at RT and freeze-thawed with liquid nitrogen 3 times to lyse the cells. To remove extracellular matrix and fat, which inhibit the PCR reaction, additional centrifugation at 12000*g* for 5 min was done. The supernatant was recovered on a new tube and mixed with chloroform (200 μL), shaken vigorously for 15 s and incubated for 3 min at RT, followed by centrifugation at 12000*g* for 15 min. The upper colorless phase was recovered on a clean tube, mixed with isopropanol (500 μL) and incubated for 10 min at RT. After centrifugation at 12000*g* for 10 min, the RNA formed a gel-like precipitate that was separated and mixed with an equal volume of ethanol. The extracted RNA was purified and eluted following the PureLink RNA Mini Kit (Invitrogen) protocol. The concentration of the extracted mRNA solutions was determined using a NanoPhotometer N60/N50 (Implen) measuring the absorbance of the samples at 260 nm and evaluating their purity by the A260/A280 and A260/A230 absorbance ratios. To carry on the synthesis of cDNA, the High-Capacity RNA-to-cDNA Kit (Applied Biosystem) was used, following the manufacturer's instructions on a 20 μL reaction. The program consisted of an incubation period of 60 min at 37 °C followed by an annealing step at 95 °C for 5 min. To perform the RT-PCR experiment, reverse and forward primer 100x solutions (10 μL) were diluted in molecular-grade water (980 μL). The nucleotides of the primers are specified in Table 2. Primer dilutions (8 μL) were mixed with cDNA solution (2 μL, 100 ng) and SyBR Green 2x (10 μL) in a 96-well clear reaction plate. A QuantStudio 1 thermocycler (Thermo Fisher Scientific) was used with a temperature set-up of a first step at 50 °C for 2 min and 95 °C for 2 min, and then 40 cycles with 95 °C for 15 s and 60 °C for 1 min. C_t values of each sample were determined and employed in the comparative C_t method to calculate the relative gene expression and the gene expression fold change was calculated relative to the expression of the target gene on hMSC prior to the experiment. GAPDH was used as the housekeeping gene.

Measurements of ALP activity: After 7 days of culture, cell culture media (500 μL) was collected and directly analyzed following the Alkaline Phosphatase Assay Kit (ab83369, Abcam) manufacturer's instructions. The absorbance of the solutions was measured at 405 nm on a BioTek Synergy Neo2 Hybrid Multimode Reader (Agilent) and the ALP activity of each sample was determined using the standard curve values.

Mechanical analysis: After 24 h and 28 days of culture, the tissue-engineered constructs (n = 3) were fixed with a 4 % PFA solution in PBS for 20 min and rinsed 3 times with DPBS. The compressive moduli of the scaffolds were determined from stress-strain curves recorded on a thermoanalyzer DMA Tritec-2000 (Triton Technology Ltd.) applying an initial compression force of 0.001 N and a final compression static force of 0.5 N, with a displacement of 0.001 mm, a frequency of 1.0 Hz, and until 80 % strain was reached. All samples were fixed and measured under the same conditions.

Statistical Analysis: Statistical significance was performed employing GraphPad Prism 8 software. For GMS diameter, measurements of microporosity and cell proliferation experiments one-way analysis of variance (ANOVA) with *posthoc* Tukey's multiple comparison tests; (****) $p < 0.0001$, (***) $p < 0.001$, (**) $p < 0.01$, and (*) $p < 0.1$ was used. For mechanical analysis, micro-computerized tomography data, cell proliferation on differentiation experiments, ALP release, GAG deposition and gene expression experiments, two-way ANOVA with *posthoc* Tukey's multiple comparison tests; (****) $p < 0.0001$, (***) $p < 0.001$, (**) $p < 0.01$, and (*) $p < 0.1$ was used. All the results are shown as mean ± standard deviation.

Table 2
List of primers and their nucleotides used for qPCR experiments.

Gene	Fw (5′-3′)	Rv (5′-3′)
GAPDH	ATG GGG AAG GTG AAG GTC G	TAA AAG CAG CCC TGG TGA CC
COL1A1	AGG GCC AAG ACG AAG ACA TC	AGA TCA CGT CAT CGC ACA ACA
COL2A1	GGC AAT AGC AGG TTC ACG TAC A	CGA TAA CAG TCT TGC CCC ACT T
COL10A1	GAC TCC CTC CTC ACT GTC GC	AGG GAA GTC TCC CTC ACT TGT
RUNX2	AGT GAT TTA GGG CGC ATT CCT	GGA GGG CCG TGG GTT CT
BGLAP	TGA GAG CCC TCA CAC TCC TC	CGC CTG GGT CTC TTC ACT AC
ACAN	GCC TTG AGC AGT CAC CTT C	CTC TTC TAC GGG GAC AGC AG
VCAN	GCA CCT GTG TGC CAG GAT A	CAG GGA TTA GAG TGA CAT TCA TCA
SOX5	ATA AAG CGT CCA ATG AAT GCC T	GCG AGA TCC CAA TAT CTT GCT G
SOX9	TTC CGC GAC GTG GAC AT	TCA AAC TCG TTG ACA TCG AAG GT

CRediT authorship contribution statement

Sandra Ramos-Díez: Writing – review & editing, Writing – original draft, Investigation, Formal analysis, Data curation. **Luis Diaz-Gomez:** Writing – review & editing, Writing – original draft, Formal analysis, Data curation. **Maria Paulis:** Writing – review & editing, Writing – original draft, Investigation, Funding acquisition. **Sandra Camarero-Espinosa:** Writing – review & editing, Writing – original draft, Supervision, Resources, Project administration, Investigation, Funding acquisition, Conceptualization.

Declaration of competing interest

The authors declare that they have no known competing financial interests or personal relationships that could have appeared to influence the work reported in this paper.

Acknowledgements

This work was supported by the EMAKIKER grant, the RETOS grant (AEI/10.13039/501100011033-114901RA-100) of the Ministry of Science and Innovation (MICINN), State Investigation Agency (AEI) (PID2020-114901RA-I00), University of the Basque Country (GIU21/033), and the Basque Government (PIBA_2022_1_0006). The manuscript was written through the contributions of all authors. S.R-D: Conceptualization, Data curation, Methodology, Validation, Formal analysis, Investigation, Software, Writing – original draft, Writing – review & editing. L.D-G: Methodology, Software, Validation, Writing – review & editing. M.P: Funding acquisition, Writing – review & editing. S.C-E: Funding acquisition, Conceptualization, Project administration, Supervision, Validation, Resources, Writing – review & editing. All authors have approved the final version of the manuscript.

Appendix A. Supplementary data

Supplementary data to this article can be found online at https://doi.org/10.1016/j.mtbio.2025.102280.

Data availability

Data will be made available on request.

References

[1] L. Alcaide-Ruggiero, R. Cugat, J. Domínguez, Proteoglycans in articular cartilage and their contribution to chondral injury and repair mechanisms, Int. J. Mol. Sci. 24 (2023).
[2] S. Camarero-Espinosa, et al., Articular cartilage: from formation to tissue engineering, Biomater. Sci. 4 (5) (2016) 734–767.
[3] A. Daly, et al., 3D bioprinting for cartilage and osteochondral tissue engineering, Adv. Healthcare Mater. 6 (2017).
[4] Y. Campos, et al., Tissue engineering: an alternative to repair cartilage, Tissue Engineering Part B - Reviews 25 (2019) 357–373.
[5] A.R. Armiento, et al., Biomaterials for articular cartilage tissue engineering: learning from biology, Acta Biomater. 65 (2018) 1–20.
[6] L. Zhou, et al., Innovative tissue-engineered strategies for osteochondral defect repair and regeneration: current progress and challenges, Adv. Healthcare Mater. 9 (2020).
[7] C. Chung, J. Burdick, Engineering cartilage tissue, Adv. Drug Deliv. Rev. 60 (2008) 243–262.
[8] P. Abdel-Sayed, D. Pioletti, Strategies for improving the repair of focal cartilage defects, Nanomedicine 10 (2015) 2893–2905.
[9] R. Danilkowicz, et al., Histological and inflammatory cytokine analysis of osteochondral lesions of the talus after failed microfracture: Comparison with fresh allograft controls, Orthopaedic Journal of Sports Medicine 9 (2021).
[10] S. Camarero-Espinosa, et al., 3D niche-inspired scaffolds as a stem cell delivery System for the regeneration of the osteochondral interface, Adv. Mater. 36 (34) (2024) 2310258.
[11] I.A.O. Beeren, et al., Installation of click-type functional groups enable the creation of an additive manufactured construct for the osteochondral interface, Biofabrication 15 (1) (2023) 014106.
[12] A. Di Luca, et al., Toward mimicking the bone structure: design of novel hierarchical scaffolds with a tailored radial porosity gradient, Biofabrication 8 (2016).
[13] S. Camarero-Espinosa, et al., Additive manufactured, highly resilient, elastic, and biodegradable poly(ester)urethane scaffolds with chondroinductive properties for cartilage tissue engineering, Mater. Today Bio 6 (2020).
[14] S. Camarero-Espinosa, et al., Additive manufacturing of an elastic poly(ester) urethane for cartilage tissue engineering, Acta Biomater. 102 (2020) 192–204.
[15] S. Bittner, et al., Fabrication and mechanical characterization of 3D printed vertical uniform and gradient scaffolds for bone and osteochondral tissue engineering, Acta Biomater. (2019) 37–48.
[16] K. Clause, L. Liu, K. Tobita, Directed stem cell differentiation: the role of physical forces, in: Cell Communication and Adhesion, 2010, pp. 48–54.
[17] W. Wei, et al., A one-stone-two-birds strategy for osteochondral regeneration based on a 3D printable biomimetic scaffold with kartogenin biochemical stimuli gradient, Adv. Healthcare Mater. 12 (2023).
[18] L. Zhang, et al., Multileveled hierarchical hydrogel with continuous biophysical and biochemical gradients for enhanced repair of full-thickness osteochondral defect, Adv. Mater. 35 (2023).
[19] Y.F. Wang, et al., 3D-printed composite scaffold with gradient structure and programmed biomolecule delivery to guide stem cell behavior for osteochondral regeneration, Biomater. Adv. (2022) 140.
[20] I. Beeren, et al., Installation of click-type functional groups enable the creation of an additive manufactured construct for the osteochondral interface, Biofabrication 15 (2023).
[21] K. Anselme, M. Bigerelle, Role of materials surface topography on Mammalian cell response, Int. Mater. Rev. 56 (2011) 243–266.
[22] H. Rostam, et al., Impact of surface chemistry and topography on the function of antigen presenting cells, Biomater. Sci. 3 (2015) 424–441.
[23] F. McWhorter, C. Davis, W. Liu, Physical and mechanical regulation of macrophage phenotype and function, Cell. Mol. Life Sci. 72 (2015) 1303–1316.
[24] S. Di Cio, J. Gautrot, Cell sensing of physical properties at the nanoscale: mechanisms and control of cell adhesion and phenotype, Acta Biomater. 30 (2016) 26–48.
[25] A. Di Luca, et al., Tailorable surface morphology of 3D scaffolds by combining additive manufacturing with thermally induced phase separation, Macromol. Rapid Commun. 38 (16) (2017).
[26] S. Camarero-Espinosa, et al., 3D printed dual-porosity scaffolds: the combined effect of stiffness and porosity in the modulation of macrophage polarization, Adv. Healthcare Mater. 11 (1) (2022).
[27] A. Di Luca, et al., Tuning cell differentiation into a 3D scaffold presenting a pore shape gradient for osteochondral regeneration, Adv. Healthcare Mater. 5 (14) (2016) 1753–1763.
[28] S. Camarero-Espinosa, et al., Directed cell growth in multi-zonal scaffolds for cartilage tissue engineering, Biomaterials 74 (2016) 42–52.
[29] X. Mendibil, et al., High throughput manufacturing of bio-resorbable micro-porous scaffolds made of poly(L-lactide-co-ε-caprolactone) by micro-extrusion for soft tissue engineering applications, Polymers 12 (1) (2020).
[30] T. Tran, et al., Development and mechanical characterization of bilayer tubular scaffolds for vascular tissue engineering applications, J. Mater. Sci. 55 (6) (2020) 2516–2529.
[31] R.P. Duan, et al., Blending with poly(L-lactic acid) improves the printability of poly (L-lactide-co-caprolactone) and enhances the potential application in cartilage tissue engineering, ACS Omega 6 (28) (2021) 18300–18313.
[32] J. Lim, Fabrication of 3D self-assembled porous microbead-type poly(L-lactide-co-ε-caprolactone) scaffolds for tissue engineering, 3D Print. Addit. Manuf. 6 (4) (2019) 204–209.
[33] S.M. Lien, L.Y. Ko, T.J. Huang, Effect of pore size on ECM secretion and cell growth in gelatin scaffold for articular cartilage tissue engineering, Acta Biomater. 5 (2) (2009) 670–679.
[34] Q. Zhang, et al., Pore size effect of collagen scaffolds on cartilage regeneration, Acta Biomater. 10 (5) (2014) 2005–2013.
[35] T.R. Kuang, et al., Facile preparation of open-cellular porous poly(L-lactic acid) scaffold by supercritical carbon dioxide foaming for potential tissue engineering applications, Chem. Eng. J. 307 (2017) 1017–1025.
[36] A.A. Zadpoor, Bone tissue regeneration: the role of scaffold geometry, Biomater. Sci. 3 (2) (2015) 231–245.
[37] P. Han, et al., Scaffold geometry modulation of mechanotransduction and its influence on epigenetics, Acta Biomater. 163 (2023) 259–274.
[38] A. Nakas, et al., Quality risk management and quality by design for the development of diclofenac sodium intra-articular gelatin microspheres, AAPS PharmSciTech (2020).
[39] N. Negrini, et al., In vitro cell delivery by gelatin microspheres prepared in water-in-oil emulsion, in: Journal of Materials Science - Materials in Medicine, 2020.
[40] S. Sulaiman, R. Idrus, N. Hwei, Gelatin microsphere for cartilage tissue engineering: current and future strategies, Polymers (2020).
[41] Y. Hao, et al., Investigation of viscoelastic-plastic properties of fresh cemented gangue fly ash backfill slurries, in: Minerals, 2024.
[42] H.G. Yang, et al., Rheological behavior of titanium dioxide suspensions, J. Colloid Interface Sci. 236 (1) (2001) 96–103.
[43] M. Sweeney, et al., Characterizing the feasibility of processing wet granular materials to improve rheology for 3D printing, J. Mater. Sci. 52 (22) (2017) 13040–13053.
[44] L.L. Ouyang, et al., 3D printing of shear-thinning hyaluronic acid hydrogels with secondary cross-linking, ACS Biomater. Sci. Eng. 2 (10) (2016) 1743–1751.
[45] N. Paxton, et al., Proposal to assess printability of bioinks for extrusion-based bioprinting and evaluation of rheological properties governing bioprintability, Biofabrication 9 (4) (2017).
[46] L. Ribeiro, et al., Programmable granular hydrogel inks for 3D bioprinting applications, Advanced Materials Technologies 8 (16) (2023).
[47] L. del-Mazo-Barbara, M.P. Ginebra, Rheological characterisation of ceramic inks for 3D direct ink writing: a review, J. Eur. Ceram. Soc. 41 (16) (2021) 18–33.
[48] F. Mukasheva, et al., Optimizing scaffold pore size for tissue engineering: insights across various tissue types, Front. Bioeng. Biotechnol. 12 (2024).
[49] S. Peyton, et al., Use of three-dimensional spheroids of hepatocyte-derived reporter cells to study the effects of intracellular fat accumulation and subsequent cytokine exposure, Biotechnol. Bioeng. 108 (5) (2011) 1181–1193.
[50] B. Boyan, et al., Role of material surfaces in regulating bone and cartilage cell response, Biomaterials (1996) 137–146.
[51] Y. Chang, et al., A general approach for generating fluorescent probes to visualize piconewton forces at the cell surface, J. Am. Chem. Soc. (2016) 2901–2904.
[52] R. Jannat, et al., Neutrophil adhesion and chemotaxis depend on substrate mechanics, J. Phys. Condens. Matter (2010).
[53] D. Sheppard, et al., Transforming growth-factor-beta differentially regulates expression of integrin subunits in guinea-pig airway epithelial-cells, J. Biol. Chem. (1992) 17409–17414.
[54] M. Robitaille, et al., Interfacing live cells with surfaces: a concurrent control technique for quantifying surface ligand activity, ACS Appl. Bio Mater. (2021) 7856–7864.
[55] S. Hocdé, O. Hyrien, R. Waugh, Molecular accessibility in relation to cell surface topography and compression against a flat substrate, Biophys. J. (2009) 369–378.
[56] A. Olubamiji, et al., Modulating mechanical behaviour of 3D-printed cartilage-mimetic PCL scaffolds: influence of molecular weight and pore geometry, Biofabrication (2016).
[57] J. Ribeiro, et al., Structural monitoring and modeling of the mechanical deformation of three-dimensional printed poly(ε-caprolactone) scaffolds, Biofabrication (2017).
[58] L. Nguyen, et al., Engineering articular cartilage with spatially-varying matrix composition and mechanical properties from a single stem cell population using a multi-layered hydrogel, Biomaterials (2011) 6946–6952.
[59] M. Kim, et al., Enhanced nutrient transport improves the depth-dependent properties of tri-layered engineered cartilage constructs with zonal co-culture of chondrocytes and MSCs, Acta Biomater. (2017) 1–11.
[60] R. Schinagl, et al., Depth-dependent confined compression modulus of full-thickness bovine articular cartilage, J. Orthop. Res. (1997) 499–506.
[61] C. Bidan, et al., Geometry as a factor for tissue growth: towards shape optimization of tissue engineering scaffolds, Adv. Healthcare Mater. 2 (1) (2013) 186–194.
[62] P. Joly, et al., Geometry-driven cell organization determines tissue growths in scaffold pores: consequences for fibronectin organization, PLoS One 8 (9) (2013).
[63] J. Knychala, et al., Pore geometry regulates early stage human bone marrow cell tissue formation and organisation, Ann. Biomed. Eng. 41 (5) (2013) 917–930.
[64] M. Hasson, et al., Considering the cellular landscape in marrow stimulation techniques for cartilage repair, Cells Tissues Organs (2024).
[65] Z. Li, et al., Mechanical load modulates chondrogenesis of human mesenchymal stem cells through the TGF-β pathway, J. Cell Mol. Med. 14 (6a) (2010) 1338–1346.
[66] Q. Bian, et al., Mechanosignaling activation of TGFβ maintains intervertebral disc homeostasis, Bone Research 5 (1) (2017) 17008.
[67] H. Watanabe, Deciphering the role of Proteoglycans and glycosaminoglycans in health and disease aggrecan and versican: two brothers close or apart, Am. J. Physiol. Cell Physiol. (2022) C967–C976.
[68] A. Jo, et al., The versatile functions of Sox9 in development, stem cells, and human diseases, Genes & Diseases 1 (2) (2014) 149–161.

[69] H. Chen, et al., Runx2 regulates endochondral ossification through control of chondrocyte proliferation and differentiation, J. Bone Miner. Res. 29 (12) (2014) 2653–2665.
[70] P. Benya, J. Shaffer, Dedifferentiated chondrocytes reexpress the differentiated collagen phenotype when cultured in agarose gels, Cell 30 (1) (1982) 215–224.
[71] E. Darling, K. Athanasiou, Rapid phenotypic changes in passaged articular chondrocyte subpopulations, J. Orthop. Res. 23 (2) (2005) 425–432.
[72] S. Schoonraad, et al., Biomimetic and mechanically supportive 3D printed scaffolds for cartilage and osteochondral tissue engineering using photopolymers and digital light processing, Biofabrication (2021).
[73] H. Xiong, A. Rabie, U. Hagg, Mechanical strain leads to condylar growth in adult rats, Front. Biosci. 10 (2005) 65–73.
[74] C. Coyle, et al., Serum CTXii correlates with articular cartilage degeneration after anterior cruciate ligament transection or arthrotomy followed by standardized exercise, Sports Health - A Multidisciplinary Approach 4 (6) (2012) 510–517.
[75] R. LaPrade, et al., Histologic and immunohistochemical characteristics of failed articular cartilage resurfacing procedures for osteochondritis of the knee, Am. J. Sports Med. 36 (2) (2008) 360–368.
[76] A. Aldahmash, et al., Collagen types I and II distribution: a relevant indicator for the functional properties of articular cartilage in immobilised and remobilised rabbit knee joints, Folia Morphol. 74 (2) (2015) 169–175.
[77] J. Lane, C. Weiss, Review of articular-cartilage collagen research, Arthritis Rheum. 18 (1975) 553–562.
[78] J. Reboredo, et al., Investigation of migration and differentiation of human mesenchymal stem cells on five-layered collagenous electrospun scaffold mimicking native cartilage structure, Adv. Healthcare Mater. 5 (17) (2016) 2191–2198.
[79] D. Martínez-Moreno, et al., Chondro-inductive b-TPUe-based functionalized scaffolds for application in cartilage tissue engineering, Adv. Healthcare Mater. 11 (19) (2022).
[80] S. Wang, et al., 3D printed chondrogenic functionalized PGS bioactive scaffold for cartilage regeneration, Adv. Healthcare Mater. 12 (27) (2023).
[81] Y. Shen, et al., Engineering a highly biomimetic chitosan-based cartilage scaffold by using short fibers and a cartilage-decellularized matrix, Biomacromolecules 22 (5) (2021) 2284–2297.
[82] A. Moliner, et al., Restoring articular cartilage: insights from structure, composition and development, Nat. Rev. Rheumatol. 21 (5) (2025) 291–308.